Crystal chemistry of martian minerals from Bradbury Landing through Naukluft Plateau, Gale crater, Mars ⚓

Shaunna M. Morrison[1,2,*,†], Robert T. Downs[1], David F. Blake[3], David T. Vaniman[4], Douglas W. Ming[5], Robert M. Hazen[2], Allan H. Treiman[6], Cherie N. Achilles[1], Albert S. Yen[7], Richard V. Morris[5], Elizabeth B. Rampe[5], Thomas F. Bristow[3], Steve J. Chipera[8], Philippe C. Sarrazin[9], Ralf Gellert[10], Kim V. Fendrich[11], John Michael Morookian[7], Jack D. Farmer[12], David J. Des Marais[3], and Patricia I. Craig[6]

[1]University of Arizona, 1040 E 4th St, Tucson, Arizona 85721, U.S.A.
[2]Geophysical Laboratory, Carnegie Institution, 5251 Broad Branch Rd NW, Washington, D.C. 20015, U.S.A.
[3]NASA Ames Research Center, Moffett Field, California 94035, U.S.A.
[4]Planetary Science Institute, 1700 E. Fort Lowell, Tucson, Arizona 85719-2395, U.S.A.
[5]NASA Johnson Space Center, Houston, Texas 77058, U.S.A.
[6]Lunar and Planetary Institute, USRA, 3600 Bay Area Boulevard, Houston, Texas 77058, U.S.A.
[7]Jet Propulsion Laboratory, California Institute of Technology, 4800 Oak Grove Drive, Pasadena, California 91109, U.S.A.
[8]Chesapeake Energy Corporation, 6100 N. Western Avenue, Oklahoma City, Oklahoma 73118, U.S.A.
[9]SETI Institute, Mountain View, California 94043, U.S.A.
[10]University of Guelph, 50 Stone Road East, Guelph, Ontario N1G 2W1, Canada
[11]American Museum of Natural History, New York, New York 10024, U.S.A.
[12]Arizona State University, Tempe, Arizona 85281, U.S.A.

Abstract

Crystal chemical algorithms were used to estimate the chemical composition of selected mineral phases observed with the CheMin X-ray diffractometer onboard the NASA Curiosity rover in Gale crater, Mars. The sampled materials include two wind-blown soils, Rocknest and Gobabeb, six mudstones in the Yellowknife Bay formation (John Klein and Cumberland) and the Murray formation (Confidence Hills, Mojave2, and Telegraph Peak), as well as five sandstones, Windjana and the samples of the unaltered Stimson formation (Big Sky and Okoruso) and the altered Stimson formation (Greenhorn and Lubango). The major mineral phases observed with the CheMin instrument in the Gale crater include plagioclase, sanidine, $P2_1/c$ and $C2/c$ clinopyroxene, orthopyroxene, olivine, spinel, and alunite-jarosite group minerals. The plagioclase analyzed with CheMin has an overall estimated average of $An_{40(11)}$ with a range of $An_{30(8)}$ to $An_{63(6)}$. The soil samples, Rocknest and Gobabeb, have an average of $An_{56(8)}$ while the Murray, Yellowknife Bay, unaltered Stimson, and altered Stimson formations have averages of $An_{38(2)}$, $An_{37(5)}$, $An_{45(7)}$, and $An_{35(6)}$, respectively. Alkali feldspar, specifically sanidine, average composition is $Or_{74(17)}$ with fully disordered Al/Si. Sanidine is most abundant in the Windjana sample (~26 wt% of the crystalline material) and is fully disordered with a composition of $Or_{87(5)}$. The $P2_1/c$ clinopyroxene pigeonite observed in Gale crater has a broad compositional range $\{[Mg_{0.95(12)-1.54(17)}Fe_{0.18(17)-1.03(9)}Ca_{0.00-0.28(6)}]_{\Sigma2}Si_2O_6\}$ with an overall average of $Mg_{1.18(19)}Fe_{0.72(7)}Ca_{0.10(9)}Si_2O_6$. The soils have the lowest Mg and highest Fe compositions $[Mg_{0.95(5)}Fe_{1.02(7)}Ca_{0.03(4)}Si_2O_6]$ of all of the Gale samples. Of the remaining samples, those of the Stimson formation exhibit the highest Mg and lowest Fe [average $= Mg_{1.45(7)}Fe_{0.35(13)}Ca_{0.19(6)}Si_2O_6$]. Augite, $C2/c$ clinopyroxene, is detected in just three samples, the soil samples [average $= Mg_{0.92(5)}Ca_{0.72(2)}Fe_{0.36(5)}Si_2O_6$] and Windjana $(Mg_{1.03(7)}Ca_{0.75(4)}Fe_{0.21(9)}Si_2O_6)$. Orthopyroxene was not detected in the soil samples and has an overall average composition of $Mg_{0.79(6)}Fe_{1.20(6)}Ca_{0.01(2)}Si_2O_6$ and a range of $[Mg_{0.69(7)-0.86(20)}Fe_{1.14(20)-1.31(7)}Ca_{0.00-0.04(4)}]_{\Sigma2}Si_2O_6$, with Big Sky exhibiting the lowest Mg content $[Mg_{0.69(7)}Fe_{1.31(7)}Si_2O_6]$ and Okoruso exhibiting the highest $[Mg_{0.86(20)}Fe_{1.14(20)}Si_2O_6]$. Appreciable olivine was observed in only three of the Gale crater samples, the soils and Windjana. Assuming no Mn or Ca, the olivine has an average composition of $Mg_{1.19(12)}Fe_{0.81(12)}SiO_4$ with a range of 1.08(3) to 1.45(7) Mg apfu. The soil samples [average $= Mg_{1.11(4)}Fe_{0.89}SiO_4$] are significantly less magnesian than Windjana $[Mg_{1.35(7)}Fe_{0.65(7)}SiO_4]$. We assume magnetite (Fe_3O_4) is cation-deficient $(Fe_{3-x}\square_xO_4)$ in Gale crater samples [average $= Fe_{2.83(5)}\square_{0.14}O_4$; range 2.75(5) to 2.90(5) Fe apfu], but we also report other plausible cation substitutions such as Al, Mg, and Cr that would yield equivalent unit-cell parameters. Assuming cation-deficient magnetite, the Murray formation [average $= Fe_{2.77(2)}\square_{0.23}O_4$] is noticeably more cation-deficient than the other Gale samples analyzed by CheMin. Note that despite the presence of Ti-rich magnetite in martian meteorites, the unit-cell parameters of Gale magnetite do not permit significant Ti substitution. Abundant jarosite is found in only one sample, Mojave2; its estimated composition is $(K_{0.51(12)}Na_{0.49})(Fe_{2.68(7)}Al_{0.32})(SO_4)_2(OH)_6$. In addition to providing composition and abundances of the crystalline phases, we calculate the lower limit of the abundance of X-ray amorphous material and the composition thereof for each of the samples analyzed with CheMin. Each of the CheMin samples had a significant proportion of amorphous SiO_2, except Windjana that has 3.6 wt% SiO_2. Excluding Windjana, the amorphous materials have an SiO_2 range of 24.1 to 75.9 wt% and an average of 47.6 wt%. Windjana has the highest FeO_T (total Fe content calculated as FeO) at 43.1 wt%, but most of the CheMin samples also contain appreciable Fe, with an average of 16.8 wt%. With the exception of the altered Stimson formation samples, Greenhorn and Lubango, the majority of the observed

---

SO_3 is concentrated in the amorphous component (average = 11.6 wt%). Furthermore, we provide average amorphous-component compositions for the soils and the Mount Sharp group formations, as well as the limiting element for each CheMin sample.

Keywords: Mars, Gale crater, Mars Science Laboratory, CheMin, X-ray diffraction, crystal chemistry, plagioclase, olivine, pyroxene, magnetite, jarosite, alunite; Martian Rocks and Minerals: Perspectives from Rovers, Orbiters, and Meteorites

INTRODUCTION

The NASA Mars Science Laboratory (MSL) rover, Curiosity, began exploring Gale crater, Mars in August 2012 with the primary goal of assessing the planet's past and present habitability (Grotzinger 2013). To meet this objective, Curiosity is equipped with an advanced suite of scientific instruments. Among these is the Chemistry and Mineralogy (CheMin) X-ray diffractometer (Blake et al. 2012), capable of determining the mineralogy of rocks and unconsolidated sediments acquired by the rover's Sample Acquisition, Sample Processing and Handling (SA/SPaH) system (Anderson et al. 2012). As of June 2016, CheMin has measured 13 samples (2 scooped soils and 11 drilled sedimentary rocks) along Curiosity's traverse in Gale crater (Table 1). Prior to CheMin's definitive mineralogical analyses, Mars missions relied on spectral models, normative mineral calculations based on bulk sample chemical composition, or select Fe-bearing oxide phase or silicate phase and oxidation state identification by Mössbauer spectroscopy (e.g., Christensen et al. 2004a, 2004b; Clark et al. 2005; Morris et al. 2006, 2008; Ruff et al. 2008). These approaches provide important information, but cannot determine relative mineral abundance or crystal chemistry with the accuracy and precision of X-ray diffraction (XRD) and Rietveld refinement. Definitive mineralogy is critical to our understanding of early environments of formation and post-depositional diagenetic processes. Crystal-chemical analyses can provide additional detail about past martian conditions by providing estimates of cation distribution within a specific mineral or phase.

Curiosity is not equipped to directly measure the chemical composition of individual mineral phases within a multi-phase sample. However, CheMin produces XRD patterns from which each crystalline phase can be identified along with the unit-cell parameters of the major phases (Blake et al. 2012). It is important to note that zoning or variation in chemistry of a single phase is not readily detected with CheMin and, therefore, the unit-cell parameters obtained for a phase represent the average thereof. Unit-cell parameters vary with chemical composition as they respond to changes in atomic radii; therefore, measured unit-cell parameters provide quantitative mineral chemical composition (Morrison et al. 2018).

In this study, we present the methods used by the CheMin science team to calibrate XRD patterns, to estimate the chemical composition of the major mineral phases (Morrison et al. 2018), and, in conjunction with bulk elemental data from the Alpha Particle X-ray Spectrometer (APXS) (Campbell et al. 2012; Gellert et al. 2015; Thompson et al. 2016; O'Connell-Cooper 2017), to derive the composition of the amorphous components

TABLE 1. Description of Gale crater samples analyzed with CheMin

Sample	Sol[a]	Description	Formation
Rocknest	69–93	Wind-blown accumulation of unconsolidated sediment [1]	Soil[b]
John Klein	182	Fine-grained, homogenous mudstone [2]	Yellowknife Bay
Cumberland	279	Fine-grained, homogenous mudstone [2]	Yellowknife Bay
Windjana	621	Fine-grained, cross-bedded sandstone to siltstone [3]	Kimberley
Confidence Hills	759	Fine-grained mudstone [4]	Murray
Mojave2	882	Fluvial/lacustrine mudstone [4]	Murray
Telegraph Peak	908	Fluvial/lacustrine mudstone [4]	Murray
Buckskin	1060	Finely-laminated mudstone [4,5]	Murray
Big Sky	1119	Unaltered, cross-bedded sandstone [6]	Stimson
Greenhorn	1137	Altered sandstone in a fracture [6]	Stimson
Gobabeb	1280	Active wind-blown dune of unconsolidated sediment [7]	Soil[b]
Lubango	1320	Altered, cross-bedded sandstone [6]	Stimson
Okoruso	1332	Unaltered, cross-bedded sandstone [6]	Stimson

Notes: [1] Bish et al. 2013; Blake et al. 2013. [2] Grotzinger et al. 2014; Vaniman et al. 2014. [3] Treiman et al. 2016. [4] Rampe et al. 2017. [5] Morris et al. 2016. [6] Yen et al. 2017. [7] Achilles et al. 2017.
[a] Sol sample obtained by Curiosity. Sol is an abbreviation for a solar day on Mars, equivalent to 24 h, 39 min, and 35.244 s (Allison 1997).
[b] Soil comprises globally-derived dust and regional materials.

present in each sample. In addition, we describe a new procedure in which plagioclase feldspar is used as an internal standard to provide improved calibration of the instrument. This new "sample cell offset" calibration has resulted in updated unit-cell parameters and chemical composition of the phases reported in Rocknest (Bish et al. 2013; Blake et al. 2013; Dehouck et al. 2014), Yellowknife Bay (Treiman et al. 2014; Vaniman et al. 2014; Dehouck et al. 2014), and Kimberley (Treiman et al. 2016) formations. The data published herein and in Morris et al. (2016), Achilles et al. (2017), Rampe et al. (2017), and Yen et al. (2017) are the most up-to date and accurate unit-cell parameters for all samples analyzed with CheMin in Gale crater, Mars (Supplemental[1] Table 1). Additionally, since the publication of Morris et al. (2016), Achilles et al. (2017), Rampe et al. (2017), and Yen et al. (2017), we have further refined the crystal-chemical algorithms, as reported in Morrison et al. (2018), and, as a result, the chemical compositions presented here may differ slightly (within 1σ uncertainty) from those previously reported.

CHEMIN X-RAY DIFFRACTION

The CheMin X-ray diffractometer produces diffraction patterns that identify minerals in unconsolidated sediments or drilled rock samples (Blake et al. 2012). Material is sieved to <150 μm before delivery to one of the instrument's 27 reusable sample cells located within the interior of the rover (Fig. 1). The sample cells, positioned in pairs at the ends of tuning forks, hold the sample between two polymer (Kapton or Mylar) windows 175 μm apart (Fig. 2). A piezoelectric actuator drives the tuning fork at resonance, and the resulting vibration causes a convective flow of sample material through the collimated 70 μm diameter X-ray beam, thus randomizing grain orientations and minimizing orientation effects. The instrument utilizes transmission geometry with a Co X-ray source ($K\alpha$1,2 avg. λ = 1.7902758 Å). An X-ray sensitive charge-coupled device (CCD) collects two-dimensional

(2D) XRD images over 10 to 40 h of analysis. The CCD detector is operated in single-photon counting mode (the detector is read out sufficiently often that most pixels contain either no charge or charge derived from a single photon). When operated in this manner, the CCD can be used to measure the amount of charge generated by each photon (and hence its energy). Diffracted $CoK\alpha$ X-ray photons are identified by their energy and are summed to yield a 2D energy-discriminated $CoK\alpha$ diffraction pattern. The short sample-to-detector distance required for instrument miniaturization results in a 2θ (°) resolution (≤0.30°) lower than that of a full-size laboratory diffractometer (~0.03° 2θ) (https://rruff.info). The CheMin team uses a modification of GSE_ADA software (Dera et al. 2013) to convert 2D images to one-dimensional (1D) patterns with any necessary corrections for alignment bias. We use the Rietveld refinement method (Young 1993) in Materials Data Inc.'s "JADE" software to determine abundances of all crystalline phases as well as unit-cell parameters of major crystalline phases (Supplemental[1] Table 1). FULLPAT analysis (Chipera and Bish 2002, 2013) yields the XRD-determined abundance of clay minerals and amorphous components.

Mineral unit-cell parameters, abundances, and compositions were reported earlier for the Rocknest soil (Bish et al. 2013; Blake et al. 2013), the Yellowknife Bay mudstones, John Klein and Cumberland (Treiman et al. 2014; Vaniman et al. 2014; Bristow et al. 2015), and the Windjana sandstone (Treiman et al. 2016). Subsequent to these publications, the CheMin team has increased the accuracy of 1D pattern refinement through additional instrument geometry corrections and refinement of 2D-to-1D parameters, the method for which is given in the following section. Updated unit-cell parameters, abundances, and estimated chemical composition are shown here, and supersede those reported earlier (Supplemental[1] Table 1 and Tables 3–9).

SAMPLE CELL OFFSET CALIBRATION

The initial 2θ calibration was based on the measurement of a well-characterized beryl-quartz standard housed in one of CheMin's sample cells. On the basis of this measurement, the sample cell-to-CCD distance is calculated to be 18.5302 mm. When a sample is delivered from SA/SPaH, the CheMin wheel is rotated to the location of a specified reusable sample cell and clamped into place. The machining tolerance of the center of individual sample cells is ±50 μm, and this uncertainty accounts for the largest contribution to 2θ measurement error in the instrument (Fig. 2). The resulting deviation in the diffracting position, along with thermal expansion and contraction of the instrument and its components and grain motion effects within the sample cell, causes subtle shifts in 2θ resulting in a small systematic error in refined cell parameters and derived estimates of mineral composition.

To determine the offset distance for each sample cell, we developed a novel method using unit-cell parameters of Na-Ca plagioclase (<0.042 K apfu). Plagioclase is abundant in almost all CheMin martian samples measured to date, except Windjana. Published values for plagioclase unit-cell parameters (Supplemental[1] Table 2a; data table available in csv format at https://github.com/shaunnamm/regression-and-minimization) exhibit a large degree of internal consistency, especially between c and γ,
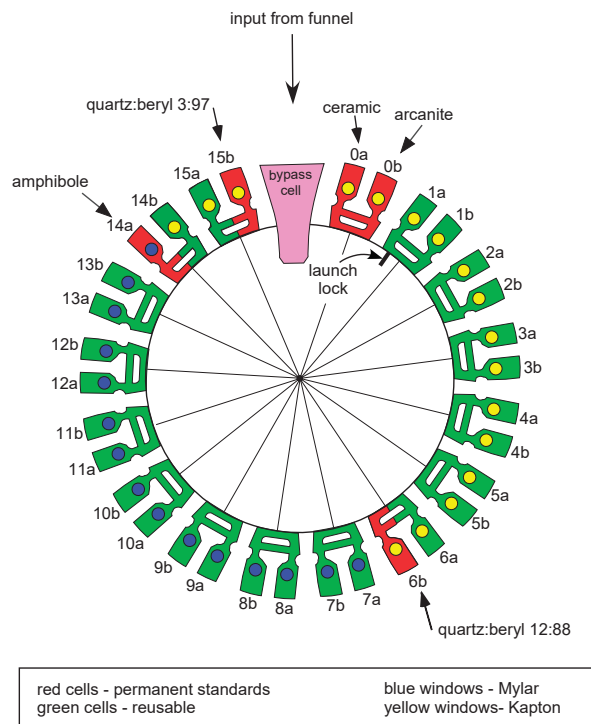
FIGURE 1. CheMin sample wheel incorporates 27 reusable sample cells and 5 calibration standards (Blake et al. 2012).
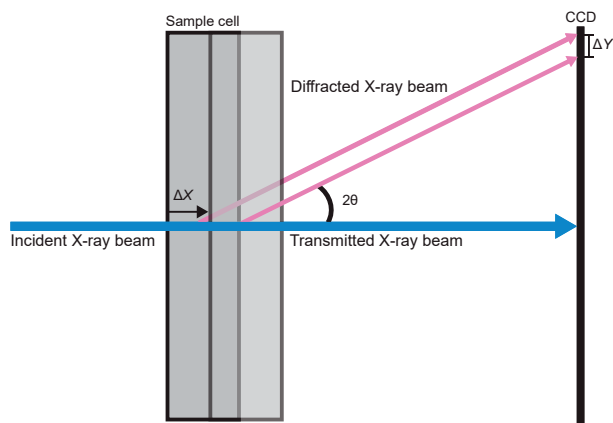
FIGURE 2. CheMin sample cell. The incident X-ray beam passes from the X-ray source, through the sample cell, and interacts with the sample material, causing X-rays to diffract and strike the CCD. The angle between the transmitted beam and the diffracted beam is 2θ. A displacement of the sample cell, resulting in an increase or decrease in sample cell-to-CCD distance, will result in an error in 2θ measurement. The angle 2θ between the transmitted and diffracted X-ray beams is invariant; however, the position of the diffracted beam on the CCD is moved laterally, resulting in an inaccurate apparent 2θ.

over the range of cell parameters observed on Mars, as evidenced by the highly correlated linear trend in Figure 3a. Significant deviations from the terrestrial c vs. γ trend are sometimes observed for CheMin-refined unit-cell parameters, such as those of Rocknest plotted on Figure 3a. In the absence of evidence to
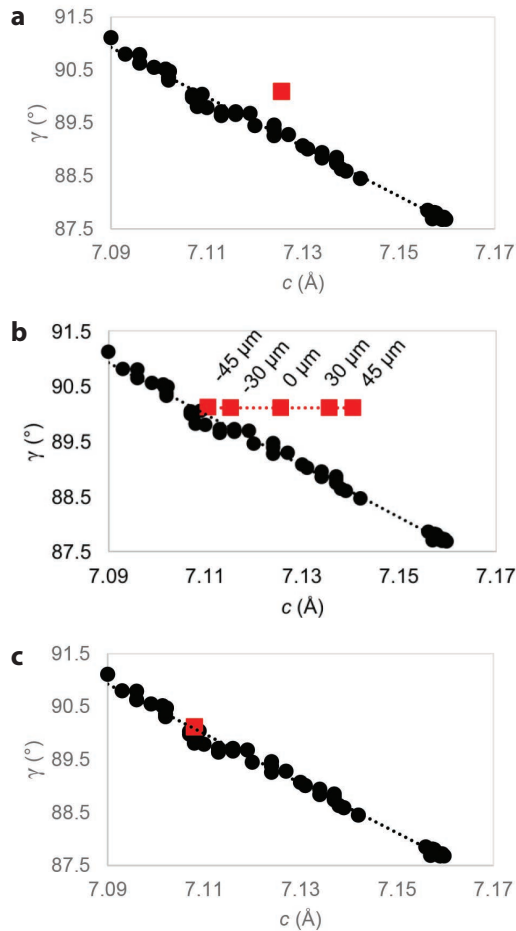
FIGURE 3. (**a**) Plagioclase *c* vs. γ unit-cell parameters. Black circles represent literature plagioclase values. The red square represents pre-calibration CheMin Rocknest plagioclase values. (**b**) Plagioclase *c* vs. γ unit-cell parameters—sample cell offset calibration. Black circles represent plagioclase data from the literature. Red squares represent refined plagioclase unit-cell parameters from the Rocknest sample with variations in sample cell-to-CCD distances from –45 to 45 μm. (**c**) Plagioclase *c* vs. γ unit-cell parameters. Black circles represent literature plagioclase values. Red square represents CheMin Rocknest plagioclase values calibrated with a sample cell offset distance of –53 μm.

demonstrate that martian plagioclase would produce a trend different from the Earth-derived relationship, we assume plagioclase on Mars should follow terrestrial trends. According to Papike et al. (2009), plagioclase/maskelynite in martian meteorites is close to the albite-anorthite join, and contains little K (K_2O 0.04 to 2.11 wt%), Fe^{3+} (Fe_2O_3 0.2 to 1.1 wt%), and Mg (MgO 0 to 0.23 wt%). Such small amounts of K, Fe, and Mg will not cause the unit-cell parameters of plagioclase to deviate from the anorthite-albite trend of Figure 3a outside its uncertainty (Morrison et al. 2018). Therefore, the variation observed in CheMin unit-cell parameters cannot be attributed to the small amounts of K, Fe, and Mg as reported in martian meteorites.

To calibrate the sample cell offset, we vary the sample-to-detector distance in the GSE_ADA software to produce

a set of diffraction patterns with the sample position moved systematically over a range of ±45 μm. Subsequently, we perform Rietveld refinements of the entire set of observed minerals, including cell parameter refinement of the major mineral phases. The refined plagioclase unit-cell parameters follow a linear trend over the offset range (Fig. 3b). The sample cell offset distance is the point of intersection between the offset trend line and the literature least-squares trend line (Table 2). Once the offset calibration is applied to the diffraction pattern, the refined plagioclase unit-cell parameters agree well with the expected trend (Fig. 3c).

Refinement of XRD patterns with calculated sample cell offsets improves the accuracy not only of plagioclase unit-cell parameters, but also of all other phases refined in CheMin samples. For example, literature unit-cell parameters of Fe-Mg olivine (Supplemental[1] Table 2b; data table available in csv format at https://github.com/shaunnamm/regression-and-minimization) vary consistently with one another (Figs. 4a–4f), just as in plagioclase, and can be used to calibrate cell offset for samples with abundant olivine. Therefore, examining Mg-Fe olivine is an independent validation of the calibration method. In CheMin samples with significant olivine and plagioclase, such as Rocknest, we observe the same internal inconsistency among olivine unit-cell parameters (Fig. 4a–4f) as we do in those of plagioclase. In the Rocknest example, olivine compositions derived individually from each of the non-calibrated unit-cell parameters produced a range of $Mg_{1.03}Fe_{0.97}SiO_4$ to $Mg_{1.54}Fe_{0.46}SiO_4$ with a standard deviation of 0.20 Mg atoms per formula unit (apfu). Applying the plagioclase sample cell offset calibration method brought the olivine unit-cell parameters into internal consistency and into agreement with terrestrial trends (Figs. 4a–4f). Additionally, the precision of olivine compositions produced by evaluation of individual unit-cell parameters vs. composition was dramatically increased, with a range of $Mg_{1.15}Fe_{0.85}SiO_4$ to $Mg_{1.18}Fe_{0.82}SiO_4$ and a standard deviation of 0.01 Mg apfu.

The plagioclase sample cell offset calibration increases the accuracy of CheMin unit-cell parameters, and hence the derived major phase composition, beyond the original expectations (Blake et al. 2012). This new calibration is employed in the CheMin results of Morris et al. (2016), Rampe et al. (2017), Yen et al. (2017), Achilles et al. (2017), and in all subsequent publications.

TABLE 2. CheMin sample cell offset distances

CheMin sample	Offset (μm)	Sample cell
Rocknest	–53	7a
Gobabeb	–38	7a
John Klein	–68	13b
Cumberland	–70	12b
Windjana	–74	13a
Confidence Hills	–74	12a
Mojave 2	–25	6a
Telegraph Peak	–45	5b
Buckskin	–76	14b
Big Sky	–26	7b
Greenhorn	–66	8a
Lubango	–75	8a
Okoruso	–28	7b

Note: Offset calculated from Oudam2, a later sample analyzed with CheMin in the former Windjana cell, 13a.
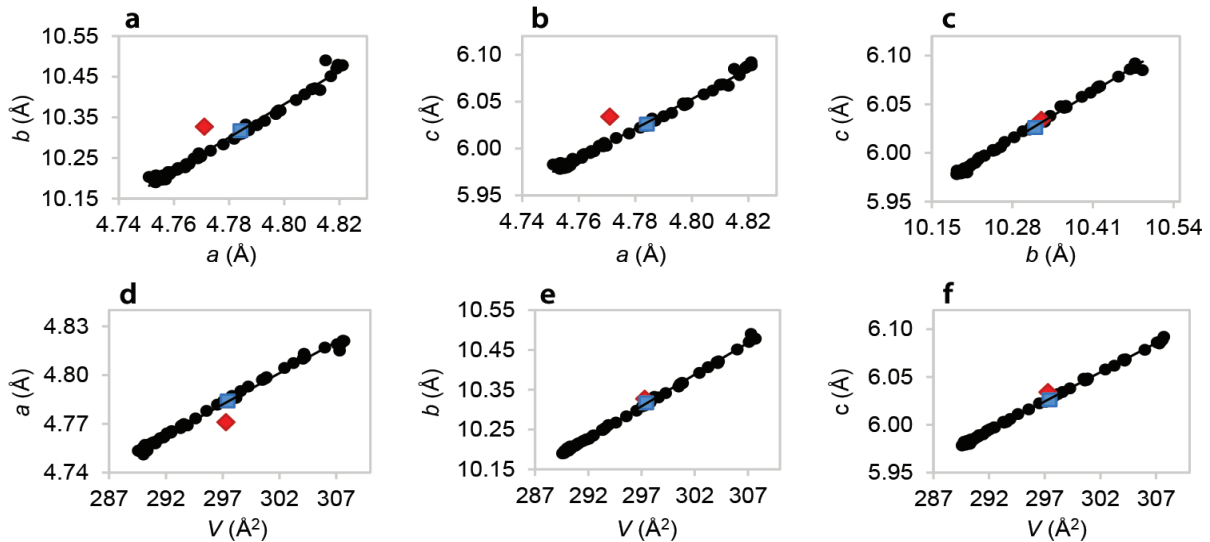
FIGURE 4. (a–f) Olivine unit-cell parameter trends. Black circles represent literature data. Red diamonds represent the pre-calibration CheMin Rocknest data. Blue squares represent the sample cell offset calibrated CheMin Rocknest data. These figures show that, despite the calibration being based solely on plagioclase, its effects produced internally consistent unit-cell parameters for the other phases.

CRYSTAL CHEMISTRY

Plagioclase and alkali feldspar

Feldspars are among the most common minerals in Earth's crust and that of other rocky bodies. The composition and ordering state of plagioclase and alkali feldspar provide important information regarding their igneous origins. Elemental substitution is common in K-feldspar (Treiman et al. 2016) and, to a lesser extent, in plagioclase. Minor chemical substitution can occur without resulting in significant deviation from observed pure K-Na or Na-Ca feldspar unit-cell parameter trends (Morrison et al. 2018). In alkali feldspar, samples with up to 0.02 Ba or Cs apfu (Angel et al. 2013) and 0.008 Rb apfu (Dal Negro et al. 1978) exhibit unit-cell parameters corresponding to pure Na-K feldspar. Sanidine can incorporate up to 0.10 Fe^{3+} apfu without showing deviation from the Na-K trend (Kuehner and Joswiak 1996; Lebedeva et al. 1993; Morrison et al. 2018). Note that up to 0.09 Fe^{3+} apfu has been observed in K-feldspar found in martian meteorite samples (Hewins et al. 2017); if this amount were to occur in Gale crater samples, it would not be detectable in the CheMin XRD data. In plagioclase, up to 0.04 K apfu (Bambauer et al. 1967) and 0.02 Fe apfu (https://rruff.info) have been reported with no deviation from the pure Na-Ca plagioclase unit-cell parameter trends. Of all measured plagioclase/maskelynite compositions from martian meteorites, 97.6% contain less than 2 wt% minor oxides (e.g., Fe_2O_3, K_2O, MgO, MnO, TiO_2, BaO) (Papike et al. 2009; Santos et al. 2015; Wittmann et al. 2015; Nyquist et al. 2016; Hewins et al. 2017), abundances that are likely to be imperceptible in unit-cell parameter trends.

Plagioclase is the most abundant crystalline phase in every Gale crater sample analyzed with CheMin, except Windjana. CheMin plagioclase compositions estimated with the crystal-chemical method detailed in Morrison et al. (2018) are shown in Table 3. The analyzed plagioclase exhibits a broad compositional

TABLE 3. CheMin plagioclase: empirical chemical formulas and associated errors (1σ)

Sample	Plagioclase formula
Rocknest	$Ca_{0.49(4)}Na_{0.51(4)}Al_{1.49}Si_{2.51}O_8$
Gobabeb	$Ca_{0.63(6)}Na_{0.37(6)}Al_{1.63}Si_{2.37}O_8$
John Klein	$Ca_{0.40(4)}Na_{0.60(4)}Al_{1.40}Si_{2.60}O_8$
Cumberland	$Ca_{0.33(5)}Na_{0.67(5)}Al_{1.33}Si_{2.67}O_8$
Windjana	$Ca_{0.17(60)}Na_{0.83(60)}Al_{1.17}Si_{2.83}O_8$
Confidence Hills	$Ca_{0.39(4)}Na_{0.61(4)}Al_{1.39}Si_{2.61}O_8$
Mojave2	$Ca_{0.41(3)}Na_{0.59(3)}Al_{1.41}Si_{2.59}O_8$
Telegraph Peak	$Ca_{0.36(3)}Na_{0.64(3)}Al_{1.36}Si_{2.64}O_8$
Buckskin	$Ca_{0.38(3)}Na_{0.62(3)}Al_{1.38}Si_{2.62}O_8$
Big Sky	$Ca_{0.52(5)}Na_{0.48(5)}Al_{1.52}Si_{2.48}O_8$
Greenhorn	$Ca_{0.40(6)}Na_{0.60(6)}Al_{1.40}Si_{2.60}O_8$
Lubango	$Ca_{0.30(8)}Na_{0.70(8)}Al_{1.30}Si_{2.70}O_8$
Okoruso	$Ca_{0.39(5)}Na_{0.61(5)}Al_{1.39}Si_{2.61}O_8$
Average	$Ca_{0.40(11)}Na_{0.60(11)}Al_{1.40}Si_{2.60}O_8$
Soil Average	$Ca_{0.56(8)}Na_{0.44(8)}Al_{1.56}Si_{2.44}O_8$
Yellowknife Bay Average	$Ca_{0.37(5)}Na_{0.63(5)}Al_{1.38}Si_{2.62}O_8$
Murray Average	$Ca_{0.38(2)}Na_{0.62(2)}Al_{1.38}Si_{2.62}O_8$
Stimson Average	$Ca_{0.40(8)}Na_{0.60(8)}Al_{1.40}Si_{2.60}O_8$
Unaltered Stimson Average	$Ca_{0.45(7)}Na_{0.55(7)}Al_{1.45}Si_{2.55}O_8$
Altered Stimson Average	$Ca_{0.35(6)}Na_{0.65(6)}Al_{1.35}Si_{2.65}O_8$

range [$An_{30(8)}$ to $An_{63(6)}$] with an average of $An_{40(11)}$. This range is compared with that of martian meteorites in Figure 5. The soil samples, Rocknest [$An_{49(4)}$] and Gobabeb [$An_{63(6)}$], exhibit notably higher Ca contents than the average plagioclase analyzed with CheMin. Plagioclase of the Murray Formation samples are very consistent with the Gale crater average and with one another [Murray average: $An_{38(2)}$]. The Stimson Formation samples show more variation [from $An_{30(8)}$ to $An_{52(5)}$], with little to no trend between the unaltered and altered samples.

Additionally, an alkali feldspar phase, sanidine, is observed in many of the CheMin samples in Gale crater (Fig. 6), with the highest abundance in Windjana [25.9(12) wt% of the crystalline material]. Estimated compositions and ordering of the alkali feldspars analyzed with the CheMin instrument in Gale crater are shown in Table 4. Alkali feldspars in Gale crater are completely disordered with compositions from $Or_{53(18)}$ to $Or_{87(5)}$ and an aver-

Plagioclase in Martian Meteorites
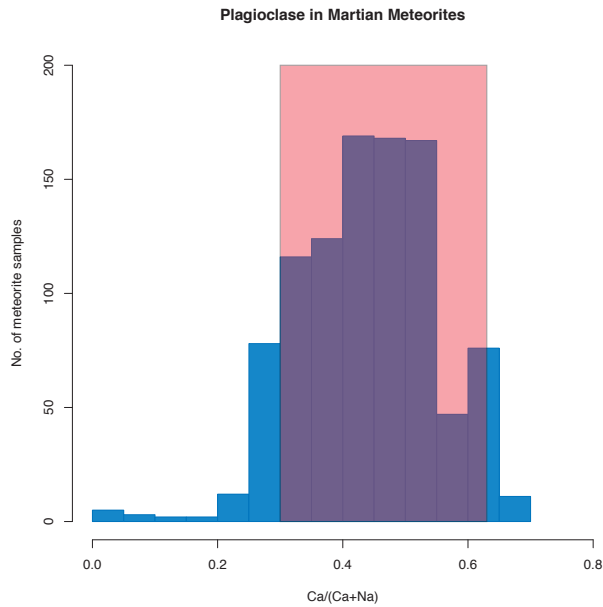
FIGURE 5. Comparison of martian meteorite plagioclase compositional distribution (blue bars) (Papike et al. 2009; Santos et al. 2015; Wittmann et al. 2015; Nyquist et al. 2016; Hewins et al. 2017) with the range of composition of plagioclase measured with CheMin (red overlay). Windjana is excluded from the range because of its extremely high uncertainty.
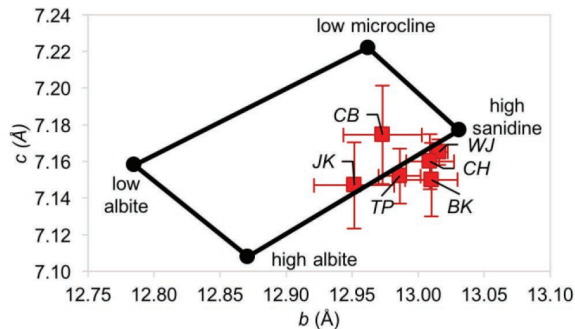
FIGURE 6. Alkali feldspar quadrilateral: composition and Al-Si ordering as a function of c and b unit-cell parameters. Black circles represent literature end-members. Red squares represent CheMin analyzed Gale crater samples with 1σ error bars: JK = John Klein, CB = Cumberland, WJ = Windjana, CH = Confidence Hills, TP = Telegraph Peak, BK = Buckskin. Composition trends from $NaAlSi_3O_8$ at the low albite–high albite edge to $KAlSi_3O_8$ at the low microcline–high sanidine edge. Al-Si ordering trends from completely ordered at the low albite–low microcline edge to completely disordered at the high albite–high sanidine edge.

age of $Or_{74(17)}$. The composition and complete Al/Si disorder of sanidine points to a high-temperature, igneous formation with no prolonged thermal history (Gupta 2015; Treiman et al. 2016).

Pyroxene

To date, CheMin has observed three pyroxene phases in Gale crater: pigeonite, $(Mg,Fe,Ca)_2Si_2O_6$, with $P2_1/c$ symmetry; augite, $(Ca,Mg,Fe)_2Si_2O_6$, with $C2/c$ symmetry; and orthopyroxene, $(Mg,Fe,Ca)_2Si_2O_6$, with $Pbca$ symmetry. The composition

TABLE 4. CheMin alkali feldspar: Empirical chemical formulas, Si-Al ordering, and associated errors (1σ)

Sample	Phase	Formula	Ordering
John Klein	sanidine	$K_{0.53(18)}Na_{0.47}Al_1Si_3O_8$	0.05(36)
Cumberland	sanidine	$K_{0.77(19)}Na_{0.23}Al_1Si_3O_8$	0.31(40)
Windjana	sanidine	$K_{0.87(5)}Na_{0.13}Al_1Si_3O_8$	−0.07(10)
Confidence Hills	sanidine	$K_{0.82(11)}Na_{0.18}Al_1Si_3O_8$	−0.10(23)
Telegraph Peak	sanidine	$K_{0.69(14)}Na_{0.31}Al_1Si_3O_8$	−0.07(22)
Buckskin	sanidine	$K_{0.76(14)}Na_{0.24}Al_1Si_3O_8$	−0.24(29)
Average		$K_{0.74(17)}Na_{0.26}Al_1Si_3O_8$	−0.02(31)
Yellowknife Bay Average		$K_{0.65(18)}Na_{0.35}Al_1Si_3O_8$	0.18(30)
Murray Average		$K_{0.76(13)}Na_{0.24}Al_1Si_3O_8$	−0.14(26)

and structure of pyroxene crystallizing from basaltic magma is sensitive to the pressure and temperature in the magma. Therefore, characterizing pyroxene phases is critical to understanding magmatic history (Turnock et al. 1973; Lindsley 1983; Papike et al. 2009). Pyroxene is commonly zoned, which may be true of the pyroxene grains in Gale crater, but, given that CheMin samples bulk material and has a slightly lower resolution than a laboratory instrument, in addition to the lack of microscopy, we have not and likely cannot detect zonation in pyroxene grains. The pyroxene structure can incorporate significant amounts of non-quadrilateral components. High-Ca (Ca mole fraction > 0.5) pyroxene in martian meteorites, however, exhibits a relatively low amount of non-quadrilateral substitution (quadrilateral components: Mg, Fe, and Ca), with 99.8% of the 876 sample analyses reported in Papike et al. (2009), Santos et al. (2015), Wittmann et al. (2015), Nyquist et al. (2016), and Hewins et al. (2017) having <10% non-quadrilateral cations. Elemental substitution occurs in low-Ca pyroxene, but to a lesser extent than in high-Ca pyroxene. Because of similarity in molar volume of the possible combinations of quadrilateral and non-quadrilateral components (Baker and Beckett 1999), it is impossible to determine a unique solution with X-ray diffraction data alone. Given the relative low frequency of non-quadrilateral substitutions in martian meteorites, we limit our investigation to the Mg-Fe-Ca pyroxene system.

Empirical formulas for pigeonite in CheMin samples are given in Table 5 and compared with martian meteorites in Figure 7. The pigeonite analyzed in Gale crater crosses a broad compositional range $\{[Mg_{0.95(12)–1.54(17)}Fe_{0.18(17)–1.03(9)}Ca_{0.00–0.28(6)}]_{\Sigma2}Si_2O_6\}$ with an average of $Mg_{1.18(19)}Fe_{0.72(7)}Ca_{0.10(9)}Si_2O_6$. Samples of the Murray formation (Confidence Hills, Mojave2, and Telegraph Peak) and the Stimson formation (Big Sky, Lubango, and Okoruso) have significantly smaller compositional ranges $\{Murray: [Mg_{1.05(23)–1.10(20)}Fe_{0.83(17)–0.94(10)}Ca_{0.00–0.07(10)}]_{\Sigma2}Si_2O_6;$ Stimson: $[Mg_{1.39(7)–1.54(17)}Fe_{0.18(17)–0.48(10)}Ca_{0.13(5)–0.28(6)}]_{\Sigma2}Si_2O_6\}$ than rock samples collected from the Gale crater plains and soil targets. Stimson pigeonite has notably high Mg and Ca content (and, therefore, low Fe) relative to the rest of the Gale samples, with the altered sample, Lubango, having the highest Mg and Ca contents of all samples measured.

Augite was detected in abundance significant enough for refinement in only three Gale crater samples: Rocknest and Gobabeb (soils) and the Windjana sandstone. Augite composition is given in Table 6 and compared with martian meteorites in Figure 7. Augites analyzed with CheMin in Gale crater fall in a narrow compositional range $\{[Mg_{0.89(8)–1.03(7)}Ca_{0.72(4)–0.75(4)}Fe_{0.21(9)–0.38(9)}]_{\Sigma2}Si_2O_6\}$, with an average of $Mg_{0.96(6)}Ca_{0.73(2)}Fe_{0.31(8)}Si_2O_6$.

TABLE 5. CheMin pigeonite: Empirical chemical formulas and associated errors (1σ)

Sample	Pigeonite formula
Rocknest	$Mg_{0.97(8)}Fe_{1.03(9)}Si_2O_6$
Gobabeb	$Mg_{0.95(12)}Fe_{0.99(17)}Ca_{0.06(8)}Si_2O_6$
John Klein	$Mg_{1.17(10)}Fe_{0.64(14)}Ca_{0.19(6)}Si_2O_6$
Cumberland	$Mg_{1.08(11)}Fe_{0.78(16)}Ca_{0.14(8)}Si_2O_6$
Windjana	$Mg_{1.29(13)}Fe_{0.70(15)}Ca_{0.01(6)}Si_2O_6$
Confidence Hills	$Mg_{1.10(9)}Fe_{0.90(9)}Si_2O_6$
Mojave2	$Mg_{1.14(16)}Fe_{0.78(22)}Ca_{0.08(10)}Si_2O_6$
Telegraph Peak	$Mg_{1.05(23)}Fe_{0.89(30)}Ca_{0.06(13)}Si_2O_6$
Big Sky	$Mg_{1.44(7)}Fe_{0.39(9)}Ca_{0.17(4)}Si_2O_6$
Lubango	$Mg_{1.54(17)}Fe_{0.18(17)}Ca_{0.28(6)}Si_2O_6$
Okoruso	$Mg_{1.39(7)}Fe_{0.48(10)}Ca_{0.13(5)}Si_2O_6$
Average	$Mg_{1.19(19)}Fe_{0.71(25)}Ca_{0.10(9)}Si_2O_6$
Soil Average	$Mg_{0.95(5)}Fe_{1.02(7)}Ca_{0.03(4)}Si_2O_6$
Yellowknife Bay Average	$Mg_{1.13(9)}Fe_{0.71(13)}Ca_{0.16(6)}Si_2O_6$
Murray Average	$Mg_{1.10(6)}Fe_{0.86(9)}Ca_{0.04(9)}Si_2O_6$
Stimson Average	$Mg_{1.45(7)}Fe_{0.35(13)}Ca_{0.19(6)}Si_2O_6$
Unaltered Stimson Average	$Mg_{1.41(4)}Fe_{0.44(6)}Ca_{0.15(3)}Si_2O_6$

TABLE 6. CheMin augite: Empirical chemical formulas and associated errors (1σ)

Sample	Augite formula
Rocknest	$Mg_{0.94(9)}Ca_{0.72(4)}Fe_{0.34(10)}Si_2O_6$
Gobabeb	$Mg_{0.89(8)}Ca_{0.73(3)}Fe_{0.38(9)}Si_2O_6$
Windjana	$Mg_{1.03(7)}Ca_{0.75(4)}Fe_{0.21(9)}Si_2O_6$
Average	$Mg_{0.96(6)}Ca_{0.73(2)}Fe_{0.31(8)}Si_2O_6$
Soil Average	$Mg_{0.92(5)}Ca_{0.72(2)}Fe_{0.36(5)}Si_2O_6$

TABLE 7. CheMin orthopyroxene: Empirical chemical formulas and associated errors (1σ)

Sample	Orthopyroxene formula
John Klein	$Mg_{0.75(8)}Fe_{1.25(8)}Si_2O_6$
Cumberland	$Mg_{0.83(8)}Fe_{1.15(10)}Ca_{0.02(5)}Si_2O_6$
Big Sky	$Mg_{0.69(7)}Fe_{1.31(7)}Si_2O_6$
Greenhorn	$Mg_{0.80(8)}Fe_{1.16(9)}Ca_{0.04(4)}Si_2O_6$
Lubango	$Mg_{0.81(10)}Fe_{1.19(11)}Si_2O_6$
Okoruso	$Mg_{0.86(20)}Fe_{1.14(20)}Si_2O_6$
Average	$Mg_{0.79(6)}Fe_{1.20(6)}Ca_{0.01(2)}Si_2O_6$
Yellowknife Bay Average	$Mg_{0.79(7)}Fe_{1.20(8)}Ca_{0.01(4)}Si_2O_6$
Stimson Average	$Mg_{0.79(7)}Fe_{1.20(7)}Ca_{0.01(2)}Si_2O_6$
Altered Stimson Average	$Mg_{0.80(5)}Fe_{1.17(5)}Ca_{0.03(3)}Si_2O_6$
Unaltered Stimson Average	$Mg_{0.77(11)}Fe_{1.23(11)}Si_2O_6$
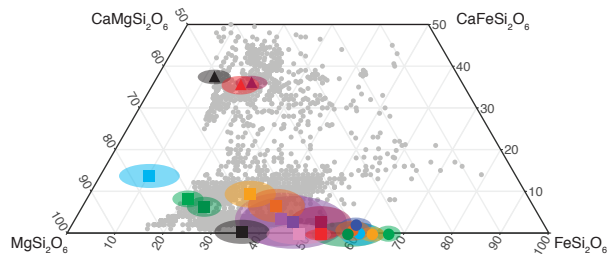
FIGURE 7. Comparison of martian meteorite pyroxene compositional distribution (gray circles) (Papike et al. 2009; Santos et al. 2015; Wittmann et al. 2015; Nyquist et al. 2016; Hewins et al. 2017) with that of the compositions observed in Gale crater pyroxene. Gale crater augite is represented as triangles, pigeonite as squares, and orthopyroxene as circles. Error ellipses are at 1σ. Red = Rocknest; dark red = Gobabeb; orange = John Klein; dark orange = Cumberland; black = Windjana; light purple = Confidence Hills; medium purple = Mojave2; dark purple = Telegraph Peak; light green = Big Sky; dark blue = Greenhorn; light blue = Lubango; dark green = Okoruso.

The chemical composition of orthopyroxene analyzed with CheMin in Gale crater is given in Table 7 and compared with martian meteorites in Figure 7. Orthopyroxene has a narrow range of $[Mg_{0.69(7)-0.86(20)}Fe_{1.14(20)-1.31(7)}Ca_{0.00-0.04(4)}]_{\Sigma2}Si_2O_6$, with an average of $Mg_{0.79(6)}Fe_{1.20(6)}Ca_{0.01(2)}Si_2O_6$.

Olivine

Mg-rich olivine, with <20 wt% Fe substituting for Mg, is the dominant mineral phase in many ultramafic rocks on Earth. It is one of the first phases to crystallize in basaltic and ultramafic melts and, as a result, it can preserve important information about the bulk rock's temperature and pressure history (Papike et al. 2009; Lee et al. 2009; Filiberto and Dasgupta 2015). On Earth, the olivine structure can accommodate significant amounts of Ca (up to 0.19 apfu) and/or Mn (up to 1 apfu) while still adhering to the Fe-Mg olivine trends in unit-cell parameters (Figs. 4a–4f). The olivine composition in martian meteorites reported by McSween and Treiman (1998), Papike et al. (2009), and Hewins et al. (2017), have less than 0.027 Ca apfu, and/or 0.038 Mn apfu (rarely with trace Ti, Cr, Ni, and/or Co). Therefore, it is likely that we can limit the range of non-Fe-Mg components in olivine analyzed with CheMin to that reported for martian meteorites.

In contrast to martian meteorites, which commonly contain olivine, only 3 of the 13 samples analyzed with CheMin contain detectable amounts of olivine. It is possible that these other 10 samples never contained olivine; however, it is more likely that they have experienced more extensive aqueous alteration during their formation or diagenesis and, given that olivine is most susceptible of the silicates to aqueous alteration, it was altered to another phase or dissolved entirely. In either scenario, this finding emphasizes the importance of recognizing that Gale crater materials are substantially different from martian meteorites, likely because of the effects of secondary weathering and alteration.

The compositions of olivine analyzed by CheMin are listed in Table 8. The average olivine composition is $Mg_{1.19(12)}Fe_{0.81(12)}SiO_4$ with a range of 1.08(3) to 1.45(7) Mg apfu. The average olivine composition of the samples analyzed in Gale crater is very similar to the average olivine composition of martian meteorites $(Mg_{1.21}Fe_{0.76}Mn_{0.02}Ca_{0.01}SiO_4)$ (Papike et al. 2009; Hewins et al. 2017) and the range is well within that of martian meteorites (Fig. 8). The Windjana sandstone has a noticeably more magnesian composition $[Mg_{1.35(7)}Fe_{0.65(7)}SiO_4]$ than that of the wind-blown soils [soil average = $Mg_{1.11(4)}Fe_{0.89(4)}SiO_4$]. Compositions of the wind-blown sediment samples, Rocknest and Gobabeb, are considered to be representative of the martian soil and to have average crustal composition, representing a global mixture of martian dust and locally or regionally derived wind-blown soil (Bish et al. 2013; Blake et al. 2013; Achilles

TABLE 8. CheMin olivine: Empirical chemical formulas and associated errors (1σ)

Sample	Olivine formula
Rocknest	$Mg_{1.14(3)}Fe_{0.86(3)}SiO_4$
Gobabeb	$Mg_{1.08(3)}Fe_{0.92(3)}SiO_4$
Windjana	$Mg_{1.35(7)}Fe_{0.65(7)}SiO_4$
Average	$Mg_{1.19(12)}Fe_{0.81}SiO_4$
Soil Average	$Mg_{1.11(4)}Fe_{0.89}SiO_4$

Olivine in Martian Meteorites
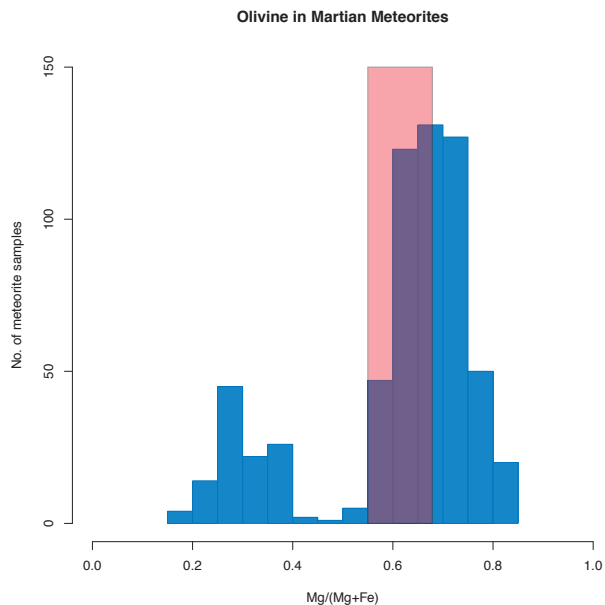
FIGURE 8. Comparison of martian meteorite Fe-Mg olivine compositional distribution (blue bars) (Papike et al. 2009; Hewins et al. 2017) with the range of composition observed in Gale crater olivine (red overlay).

et al. 2017). The similarity in composition of Rocknest [$Fo_{57(2)}$] and Gobabeb [$Fo_{54(2)}$] echoes the assertion that these unconsolidated sediments may represent average crustal composition.

Magnetite

The cubic spinel structure can accommodate Fe, Mg, Al, Ti, and various transition metals and other elements, making it impossible to determine the composition of a spinel based on the single parameter than can be determined with CheMin—the *a* cell dimension (Morrison et al. 2018). We detected a spinel phase in each of the Gale crater samples analyzed with CheMin. It is important to note that the Gale samples are rocks or loose sediment and therefore may contain spinel crystals of varying compositions; given that we cannot isolate single grains with powder X-ray diffraction, the spinel peaks, and resulting unit-cell parameters, represent an average of all spinel grains in an analyzed sample. Magnetite ($Fe^{2+}Fe_2^{3+}O_4$) or Ti-magnetite [as well as minor amount of chromite ($Fe^{2+}Cr_2O_4$)] is present in martian meteorites and was detected on the martian surface by the MER Mössbauer spectrometers, particularly at Gusev crater (Morris et al. 2006, 2008). Martian meteorites contain a significant proportion of chromite, $Fe^{2+}Cr_2O_4$ (~18% of all samples cited in Morrison et al. 2018), and much of the magnetite contains significant proportions of Al (up to 1.01 apfu, assuming no site vacancy), Ti (up to 0.95 apfu), and Mg (up to 0.43 apfu), with minor (<0.05 apfu) Si, V, Mn, Ca, Na, Ni, Co, and Zn (Morrison et al. 2018).

Given the large compositional range accommodated by the spinel structure and frequent occurrence of minor elements in martian meteorite magnetite, we explored the possible range of composition in magnetite detected in Gale crater. In Figure 9, the literature trends of Fe vs. the *a* unit-cell parameter are given
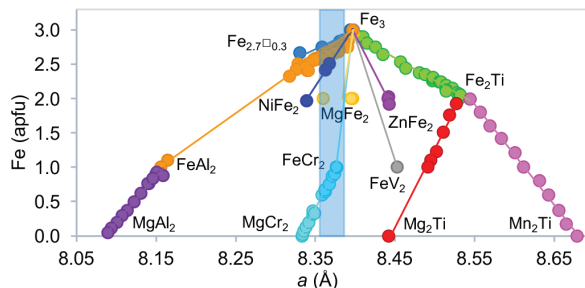
FIGURE 9. Select spinel oxide phases (M_3O_4) as a function of Fe content and *a* unit-cell parameter. The blue region represents the range of Gale crater magnetite.

for (Fe,□), (Fe,Al), (Fe,Ti), (Fe,Mg), (Fe,Cr), (Fe,Ni), (Fe,Zn), (Fe,V) (Fe,Al,□), (Fe,Mg,Al), (Fe,Mn,Ti), (Fe,Mg,Cr), and (Fe,Mg,Ti) spinel oxide phases. The complexity of Figure 9, a result of variation in cation size, site occupancies, and oxidation state of multi-element composition, illustrates that numerous chemical combinations can produce a given *a* cell edge in the spinel structure.

Based on the unit-cell dimensions refined with CheMin, in combination with meteorite and mission data, we assume that most of the spinels analyzed with CheMin in Gale crater can be ascribed to a solid solution between pure magnetite (Fe) and cation-deficient magnetite (Fe,□), which gives an average composition of $Fe_{2.83(5)}\square_{0.14}O_4$ and a range of 2.75(5) to 2.90(5) Fe per formula unit. However, other reasonable substitutions for Fe could produce the unit-cell parameter of the Gale crater spinels, such as Al, Mg, and Cr, each of which have implications on the environment of formation. As detailed in Treiman et al. (2016), chromite or chromian magnetite is a common accessory phase in basalt, while cation-deficient magnetite is often associated with the diagenetic oxidation of olivine, and significant amounts of Mg in magnetite are associated with rare geologic settings (impact spherules, meteorite fusion crusts, rare carbonatites) that are unlikely in general for the Gale crater materials. Ti is a common substituent in magnetite formed on Earth and found in martian meteorites, but the Gale crater refined unit-cell dimensions are too small for a significant (>0.08 apfu) Ti substitution (Fig. 9). Chromite or heavily Cr-enriched magnetite fits the geologic setting of Gale crater, but elevated amounts are not detected in bulk sample analysis, making such a composition unlikely (Treiman et al. 2016). Therefore, it is most likely that the spinel phases observed in Gale are mixtures of magnetite to cation-deficient magnetite, possibly with minor amounts of Al, Mg, Cr, and/or chromite.

Proposed magnetite compositions of Gale crater samples analyzed with CheMin are given in Table 9. The unit-cell dimension, and resulting estimated compositions, are relatively similar across the Gale crater samples, with the exception of the Murray formation samples, which have notably smaller unit-cell dimensions and, therefore, if we assume a magnetite to cation-deficient magnetite composition, are distinctly more cation deficient (average: $Fe_{2.77(2)}\square_{0.23}O_4$) than the Gale crater average and even more so than the Stimson formation samples (Average: $Fe_{2.88(2)}\square_{0.12}O_4$).

TABLE 9. CheMin magnetite: Empirical chemical formulas and associated errors (1σ)

	$Fe_{3-x}\square_xO_4$		$FeAl_2O_4$		$Fe_{1-x}Al_{2-y}\square_{x+y}O_4$			$(FeMgCr^{3+})_{\Sigma 2}O_4$		
	Fe	$\square$	Fe	Al	Fe	Al	$\square$	Fe	Mg	Cr
Rocknest	2.86(5)	0.14	2.87(4)	0.13	2.76(5)	0.11(6)	0.13(8)	–	–	–
Gobabeb	2.86(6)	0.14	2.86(7)	0.14	2.76(7)	0.11(7)	0.13(9)	–	–	–
John Klein	2.82(5)	0.18	2.79(3)	0.21	2.71(4)	0.14(6)	0.16(7)	0.89(5)	0.11(5)	2.00(7)
Cumberland	2.81(5)	0.19	2.77(3)	0.23	2.69(4)	0.15(6)	0.16(7)	0.82(5)	0.18(5)	2.00(7)
Windjana	2.83(5)	0.17	2.80(2)	0.20	2.71(4)	0.14(6)	0.15(7)	0.91(3)	0.09(3)	2.00(5)
Confidence hills	2.79(5)	0.21	2.74(3)	0.26	2.66(5)	0.16(6)	0.18(8)	0.73(7)	0.27(7)	2.00(10)
Mojave2	2.76(5)	0.24	2.67(3)	0.33	2.61(4)	0.19(6)	0.20(7)	0.55(5)	0.45(5)	2.00(7)
Telegraph Peak	2.75(5)	0.25	2.65(2)	0.35	2.60(4)	0.20(6)	0.20(7)	0.51(3)	0.49(3)	2.00(5)
Buckskin	2.77(5)	0.23	2.69(2)	0.31	2.62(4)	0.19(6)	0.19(7)	0.60(3)	0.40(3)	2.00(5)
Big Sky	2.90(5)	0.10	2.93(2)	0.07	2.82(4)	0.08(6)	0.11(7)	–	–	–
Greenhorn	2.89(5)	0.11	2.92(2)	0.08	2.80(4)	0.08(6)	0.11(7)	–	–	–
Lubango	2.86(5)	0.14	2.86(3)	0.14	2.76(5)	0.11(6)	0.13(8)	–	–	–
Okoruso	2.87(5)	0.13	2.89(2)	0.11	2.78(4)	0.10(6)	0.12(7)	–	–	–
Average	2.83(5)	0.17	2.80(9)	0.20	2.71(7)	0.14(4)	0.15(3)	0.72(15)	0.28(15)	2.00(1)
Soil Average	2.86(3)	0.14	2.86(3)	0.14	2.76(3)	0.11(3)	0.13(4)	–	–	–
Yellowknife Bay Average	2.82(4)	0.18	2.78(2)	0.22	2.70(4)	0.14(4)	0.16(5)	0.60(8)	0.40(8)	2.00(2)
Murray Average	2.77(2)	0.23	2.69(4)	0.31	2.62(4)	0.19(2)	0.19(2)	0.60(8)	0.40(8)	2.00(2)
Stimson Average	2.88(2)	0.12	2.90(3)	0.10	2.79(4)	0.09(2)	0.12(2)	–	–	–
Unaltered Stimson Average	2.88(3)	0.12	2.91(3)	0.09	2.79(3)	0.09(3)	0.12(4)	–	–	–
Altered Stimson Average	2.87(3)	0.13	2.89(3)	0.11	2.78(3)	0.10(3)	0.12(4)	–	–	–

Alunite-jarosite

The discovery of alunite-jarosite group minerals on Mars has important implications for ancient martian weathering environments (Klingelhöfer et al. 2004; Zolotov and Shock 2005; Morris et al. 2006; Golden et al. 2008; Swayze et al. 2008; Mills et al. 2013; Hurowitz et al. 2017). Alunite-jarosite group minerals include alunite, $KAl_3(SO_4)_2(OH)_6$; jarosite, $KFe_3^{3+}(SO_4)_2(OH)_6$; natroalunite, $NaAl_3(SO_4)_2(OH)_6$; natrojarosite, $NaFe_3^{3+}(SO_4)_2(OH)_6$; ammonioalunite, $NH_4Al_3(SO_4)_2(OH)_6$; ammoniojarosite, $NH_4Fe_3^{3+}(SO_4)_2(OH)_6$; and hydroniumjarosite, $(H_3O)Fe_3^{3+}(SO_4)_2(OH)_6$. Figure 10 shows the cell parameters of the "jarosite" detected in the Mojave2 sample plotted on the alunite-jarosite quadrilateral (Morrison et al. 2018). The refined unit-cell parameters correspond to a jarosite composition of $(K_{0.51(12)}Na_{0.49})(Fe_{2.68(7)}Al_{0.32})(SO_4)_2(OH)_6$. The uncertainties reported here for the jarosite compositions are inaccurately low because the equations used to calculate the alunite-jarosite compositions only incorporate uncertainty from the unit-cell parameters and not the uncertainty of the natural mineral system.
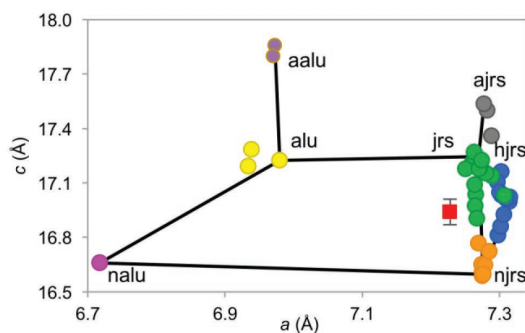
FIGURE 10. Alunite-jarosite group minerals as a function of the *a* and *c* unit-cell parameters. The CheMin Mojave2 sample unit-cell parameters are represented by the red square and correspond to a composition of $(K_{0.51(12)}Na_{0.49})(Fe_{0.89(2)}Al_{0.11})(SO_4)_2(OH)_6$. Abbreviations: jrs = jarosite, alu = alunite, njrs = natrojarosite, nalu = natroalunite, ajrs = ammoniojarosite, aalu = ammonioalunite, hjrs = hydroniumjarosite.

PETROLOGIC INTERPRETATIONS: MAFIC MINERALS

Determining the mineral chemistry of mafic minerals has direct implications for the interpretation of soils and rocks in Gale crater. As an example of the petrologic value of these determinations, we consider the species and composition of the pyroxene and olivine phases observed in Gale crater. Figures 11a–11c show the compositional ranges for pyroxene and olivine, as given in Tables 5 to 8, plotted on a conventional pyroxene quadrilateral diagram. Also shown are the low-pressure ($P < 2$ kbar) temperature contours and three-phase triangles (orthopyroxene + pigeonite + augite) in 100 °C intervals from Lindsley (1983). Note that for a pyroxene to be correctly plotted with respect to the isotherms requires that the effects of non-quadrilateral components in the pyroxene be accounted for via the projection scheme reported in Lindsley (1983). Although this is not a correction we can make (since, as discussed above and in Morrison et al. 2018, the proportions of non-quadrilateral components in the pyroxenes analyzed with CheMin in Gale crater cannot be calculated from their unit-cell parameters), by analogy with the compositions of pyroxenes in martian meteorites, we assume that pyroxenes observed in Gale crater also have relatively minor abundances of non-quadrilateral constituents and, thus, the temperature error associated with their uncorrected placement on the quadrilateral is likely to be low. Olivine compositions are plotted below the enstatite-ferrosilite join at the appropriate Fe/Mg ratios. For olivines with Mg/(Mg+Fe) like those in Gale crater (~0.54–0.68, Fig. 8), equilibrium orthopyroxenes have similar Fe/Mg ratios and, in this compositional range, the olivine-orthopyroxene Fe-Mg exchange coefficient is nearly independent of temperature (Sack 1980). Figures 11a–11c include all of the applicable samples analyzed with CheMin, and support several significant petrologic inferences, including: (1) comparisons and possible consanguinity of materials, (2) evidence for single or multiple sediment sources, (3) changes in sediment provenance, and (4) effects of chemical alteration.

(1) Pyroxene and olivine compositions can provide crucial clues to the consanguinity of samples. Consider the mafic minerals of the two analyzed sands, Rocknest and Gobabeb (Fig. 11a). Rocknest is a sand shadow analyzed very early in the mission
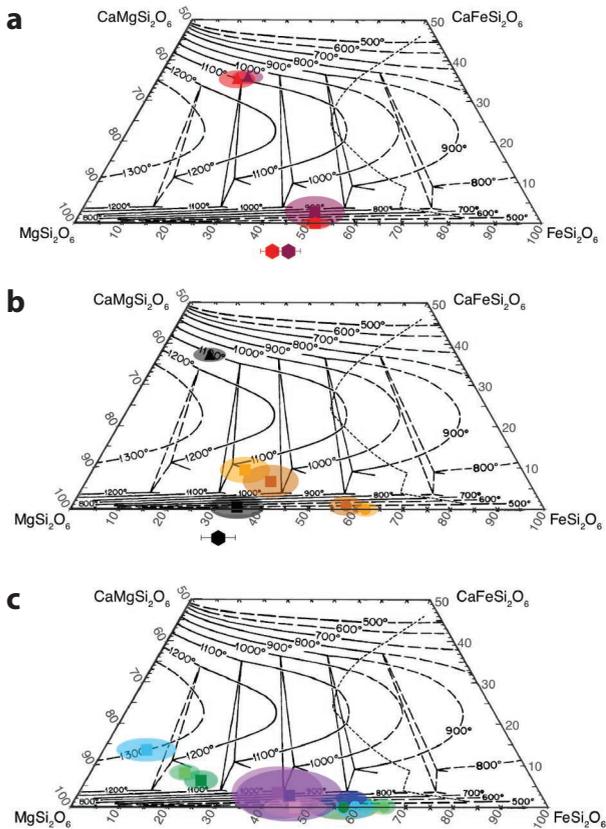
FIGURE 11. Pyroxene quadrilateral (Lindsley 1983) plotted with augite, pigeonite, and olivine chemical composition from CheMin. Error ellipses are at 1σ. The straight lines are joins between equilibrium pyroxene compositions, and include the equilibrium Fe-Mg partitioning between the various pyroxenes. Contours represent temperature of formation at 100 °C intervals. Olivine compositions are plotted below the enstatite-ferrosilite join at the appropriate Fe/Mg ratios. (**a**) Wind-blown soils, Rocknest, and Gobabeb. Augite is represented as triangles, pigeonite as squares, and olivine as hexagons. Red = Rocknest and dark red = Gobabeb. (**b**) Yellowknife Bay, John Klein, and Cumberland, as well as the Windjana sandstone. Augite is represented as triangles, pigeonite as squares, and olivine as hexagons. Orange = John Klein, dark orange = Cumberland, and black = Windjana. (**c**) Murray formation (Confidence Hills, Mojave2, and Telegraph Peak in shades of purple) and the Stimson formation (unaltered Big Sky and Okoruso in shades of green; altered Greenhorn and Lubango in shades of blue). Pigeonite is represented as squares and orthopyroxene as circles. Light purple = Confidence Hills, medium purple = Mojave2, dark purple = Telegraph Peak, light green = Big Sky, dark blue = Greenhorn, light blue = Lubango, and dark green = Okoruso.

(Blake et al. 2013); Gobabeb is a sample of the active Namib sand dune, part of the Bagnold Dune Field, ~10 km distant from Rocknest (Achilles et al. 2017). Figure 11a shows that the pyroxenes and olivine observed in Rocknest and Gobabeb have identical compositions within uncertainties, which suggests that both represent the same sand mass, however, the distinctly different plagioclase compositions (An$_{49(4)}$ and An$_{63(6)}$ in Rocknest and Gobabeb, respectively) suggest the possibility of different parentage over time (Achilles et al. 2017). Similarly, the adjacent samples John Klein and Cumberland (Fig. 11b), both drilled in

the Yellowknife Bay area, have pyroxenes with identical compositions (within uncertainty). This result is expected but still encouraging, as these two drill samples were within meters of each other in the same stratigraphic horizon. In another example, the drill samples Confidence Hills, Mojave2, and Telegraph Peak (Fig. 11c) were taken within a few meters of stratigraphy in a single section of the Murray mudstone formation (Rampe et al. 2017). The pigeonites in those samples (the only mafic mineral present) have identical composition within uncertainty, consistent with their common stratigraphic positions.

(2) Chemical equilibria (or lack thereof) among the mafic minerals can suggest whether a sediment had a single basalt source or multiple sources. Mafic minerals (olivine, low-Ca pyroxene, and high-Ca pyroxene) in the sand samples Rocknest and Gobabeb have widely differing Fe/Mg ratios, and thus are consistent with several basaltic sources (Fig. 11a), as might be reasonable for a regional sand sheet such as the current Bagnold Dunes. However, this interpretation is not certain, as this range of mineral compositions could have formed in a single igneous rock as it evolved during crystallization—the magnesian augite forming first, and the less magnesian pigeonite forming later, at lower temperatures. A similar pattern, though not identical, is seen in the nakhlite martian meteorites (Treiman 2005). In those basaltic rocks, augite and olivine were the early-crystallizing mafic silicates, and were followed much later by pigeonite and orthopyroxene, both significantly more ferroan than the augite. A similar trend in pyroxene and olivine is observed in the Windjana drill sample, Figure 11b. The chemical compositions of the rocks near Windjana (the Kimberley area) imply several sediment sources (Treiman et al. 2016; Le Deit et al. 2016; Treiman and Medard 2016; Siebach et al. 2017).

(3) Mafic minerals can be strong indicators of changing sediment sources (i.e., provenance). Take, for example, the contrast between the mineralogy of the Murray mudstone samples (Confidence Hills, Mojave2, and Telegraph Peak; Rampe et al. 2017) and the mineralogy of the overlying Stimson sandstone (Big Sky, Greenhorn, Lubango, and Okoruso; Yen et al. 2017). The mafic mineralogy of those two sample groups is quite different (Fig. 11c): the Murray mudstones (in shades of purple) having only pigeonite of very low Ca content and intermediate Fe/Mg ratio, while the Stimson sandstone (shades of blue and green) contains magnesian, relatively high-Ca pigeonite and very ferroan orthopyroxene (approaching ferrosilite composition). Clearly, these sediments are not closely related, and stratigraphic studies along Curiosity's traverse have demonstrated the presence of an unconformity, with significant topographic relief, between the Murray and Stimson (Watkins et al. in revision).

(4) The mafic mineralogy of a sediment can record evidence about the chemical processes of its diagenesis and alteration. There is extensive evidence of widespread, though volumetrically minor, chemical alteration and diagenesis of sediments in Gale crater, including formation of smectitic clay from olivine (Vaniman et al. 2014; Bristow et al. 2015), acid-sulfate alteration to produce jarosite-group minerals among others (Rampe et al. 2017), and silicification surrounding fractures (Yen et al. 2017). Any of these alteration processes could affect the mafic silicate minerals of the sediments. John Klein and Cumberland have been sufficiently weathered such that all or most of the olivine

that was likely present in the source material has altered to a smectitic clay (Vaniman et al. 2014). The Murray mudstones of Pahrump Hills (Rampe et al. 2017) have been altered by varying degrees of acid-sulfate solutions, also resulting in the complete loss of any original olivine. The silicified Stimson sandstones, Greenhorn and Lubango, have orthopyroxene compositions similar to those of their unsilicified counterparts, Big Sky and Okoruso. The abundance of pigeonite in altered Stimson samples is much diminished (5 to 6 wt% of the crystalline material) compared to the unaltered samples (21 wt% crystalline), and the composition of the remaining pigeonite (especially in Lubango) is noticeably more magnesian than that of the unaltered samples nearby (Fig. 11c). However, note that pigeonite is so near the detection limit in the altered Stimson samples that the unit-cell parameters of Greenhorn could not be accurately refined and the uncertainty of the unit-cell parameters and resulting estimated composition of Lubango is high. Therefore, it is difficult to make an accurate comparison of unaltered vs. altered Stimson pigeonite composition.

BULK COMPOSITION OF AMORPHOUS MATERIALS

All martian rocks and soils examined with CheMin contain significant amounts of X-ray amorphous material, ranging from 20 to 64 wt%. The amorphous and clay mineral components of Gale crater samples are measured and modeled using the full pattern fitting program FULLPAT (Chipera and Bish 2002, 2013). Sample patterns and reference intensity ratios (RIRs) from a suite of natural and synthetic amorphous and clay mineral samples are measured in a CheMin-equivalent CheMin IV instrument at NASA Johnson Space Center. The amorphous component(s) in the Mars samples are identified and modeled by fitting these known and measured library patterns to the Mars data. The characterization of amorphous materials using X-ray diffraction alone is problematic because such materials lack the translational periodicity needed to produce sharp diffraction peaks. However, limits on the bulk amorphous material composition and proportion in a given sample can be estimated by comparing its bulk elemental composition from the APXS (Campbell et al. 2012; Gellert et al. 2015; Thompson et al. 2016; O'Connell-Cooper 2017) with that of its crystalline component from CheMin (see below). For each sample, the APXS instrument measures the <150 µm post-sieved material dumped onto the martian surface by SA/SPaH after analyses with CheMin are complete. This is the same reservoir of material from which CheMin obtains its sample.

We estimated the chemical composition of amorphous material at the lower limit of its proportion with the following matrix equation:

$$\mathbf{A} = \mathbf{B} - \alpha\mathbf{C}, \tag{1}$$

where $\mathbf{A}$ is the X-ray amorphous component composition; $\mathbf{B}$ is the bulk sample composition measured by APXS; α is a scalar that corresponds to the maximum possible fraction of crystalline material in a sample constrained by mass balance; and $\mathbf{C}$ is the bulk crystalline composition (Supplemental[1] Table 3).

We calculate bulk crystalline composition by summing the crystal-chemically derived major phase compositions and the ideal chemical compositions of the minor crystalline phases,

with each phase scaled in proportion to its estimated abundance, determined by Rietveld refinement (Supplemental[1] Table 3 and Tables 10a–10e). Alpha (Tables 10a–10e) is calculated by scaling and subtracting the crystalline composition from the APXS-measured bulk composition until an element in the bulk composition is driven to zero. The limiting element in the soil samples is Mg and the limiting element of the Yellowknife Bay formation, Buckskin, and the altered Stimson formation samples is Al; however, the remaining Gale samples are limited by either Ca or K, with no apparent trend among the samples or formations.

In contrast to α, which is derived from chemical composition, the amorphous-component proportion estimated by FULLPAT is derived solely from the diffracted intensities of the crystalline and amorphous materials in the XRD pattern. Figure 12 compares the minimum proportion of amorphous material (i.e., $1 - \alpha$) vs. the FULLPAT estimated amorphous-component proportion for each of the CheMin samples (Blake et al. 2013; Treiman et al. 2014, 2016; Vaniman et al. 2014; Morris et al. 2016; Achilles et al. 2017; Rampe et al. 2017; Yen et al. 2017). The method presented herein produces an estimate of the maximum proportion of crystalline material and, consequently, the minimum amount of amorphous material (Tables 10a–10e). It is critical to point out that this method does not account for minor or trace elements that are not solved for in our crystal-chemical estimation of major phase composition (Morrison et al. 2018) nor does it account for departure from the ideal composition of minor phases. The elements Mn, Cr, Al, and Ti are of particular concern because they are commonly minor components in pyroxene, olivine, and/or magnetite (see previous section).

X-ray amorphous materials may contain crystalline phases present at quantities below the detection limit of CheMin (<1 to 3 wt%) and/or materials that do not coherently diffract X-rays (e.g., amorphous or short-range ordered materials). The composition and proportion of amorphous material in a sample provide important information regarding the nature of the source material and post-depositional processes. These materials may contain many components, including allophane/hisingerite, mafic glass, felsic glass, Opal-A and Opal CT, short-range ordered (SRO) sulfates, and nanophase iron oxides (Morris et al. 2006, 2008, 2016; Bish et al. 2013; Blake et al. 2013; Rampe et al. 2014;
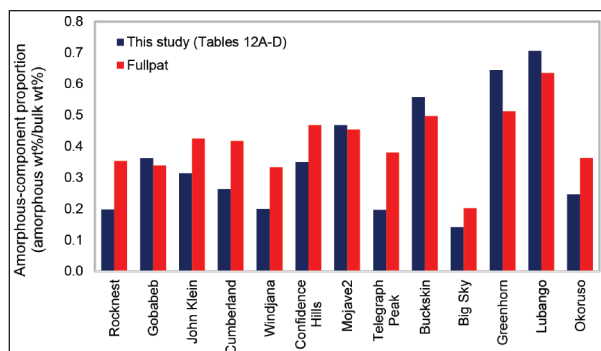
FIGURE 12. Comparison of the minimum possible proportion of amorphous material calculated by mass balance from measured composition (this study) vs. an estimate of the amorphous-component proportion by full pattern fitting (FULLPAT) of the diffracted intensities of the amorphous material.

TABLE 10A. CheMin sample APXS, amorphous (normalized), and crystalline (normalized) compositions, in oxide wt%: Martian soil samples

	Rocknest			Gobabeb			Soil Average		
	APXS	Xtal	Amorph	APXS	Xtal	Amorph	APXS	Xtal	Amorph
SiO_2	42.97	47.663	24.42	47.88	46.359	50.583	45.425	47.011	37.502
TiO_2	1.19	0.74	3.003	0.88	0	2.42	1.035	0.37	2.711
Al_2O_3	9.37	11.427	1.179	9.78	11.188	7.326	9.575	11.308	4.253
Cr_2O_3	0.49	0	2.458	0.39	0	1.072	0.44	0	1.765
FeO_T	19.18	18.199	23.237	17.91	18.797	16.375	18.545	18.498	19.806
MnO	0.424	0	2.126	0.367	0	1.009	0.395	0	1.568
MgO	8.69	10.87	0	7.57	11.903	0	8.13	11.387	0
CaO	7.26	7.925	4.64	7.3	9.46	3.53	7.28	8.692	4.085
Na_2O	2.7	2.409	3.883	2.75	1.527	4.892	2.725	1.968	4.387
K_2O	0.49	0	2.458	0.49	0	1.347	0.49	0	1.903
P_2O_5	0.95	0	4.766	0.79	0	2.172	0.87	0	3.469
SO_3	5.47	0.767	24.366	3.36	0.767	7.898	4.415	0.767	16.132
Cl	0.69	0	3.462	0.5	0	1.375	0.595	0	2.418
F	–	–	–	–	–	–	–	–	–
H_2	–	–	–	–	–	–	–	–	–
Proportion[a]	–	0.80246	0.19754	–	0.63764	0.36236		0.72005	0.27995

Notes: All normalized sums total 100 wt%. The proportion is the minimum (lower limit) of amorphous material and maximum (upper limit) of crystalline material in a sample, based on mass-balance.

[a] These proportions represent the maximum possible proportion of crystalline material (upper limit) and, consequently, the minimum proportion of amorphous material (lower limit). Bulk crystalline and amorphous component compositions computed with FULLPAT-estimated proportions are reported in Achilles et al. (2017).

TABLE 10B. CheMin sample APXS, amorphous (normalized), and crystalline (normalized) compositions, in oxide wt%: Yellowknife Bay and the Kimberley formations

	John Klein			Cumberland			Windjana		
	APXS	Xtal	Amorph	APXS	Xtal	Amorph	APXS	Xtal	Amorph
SiO_2	41.06	44.866	33.007	41.13	46.929	25.557	37.38	46.482	3.614
TiO_2	1.05	0	3.287	0.99	0	3.659	1.07	0	5.174
Al_2O_3	8.51	12.511	0	8.63	11.837	0	5.62	6.098	3.936
Cr_2O_3	0.47	0	1.471	0.46	0	1.7	0.49	0	2.369
FeO_T	20.68	20.592	20.894	21.95	23.414	18.033	27.9	24.088	43.116
MnO	0.325	0	1.018	0.294	0	1.086	0.552	0	2.667
MgO	8.97	6.832	13.535	9.32	6.276	17.534	12.29	10.941	17.735
CaO	7.87	7.267	9.164	6.66	5.009	11.119	5.26	6.53	0.552
Na_2O	2.93	3.251	2.25	3.01	3.513	1.658	0.96	0.946	1.036
K_2O	0.55	0.4	0.87	0.62	0.653	0.532	3.09	3.921	0
P_2O_5	0.92	0	2.88	0.86	0	3.179	0.64	0	3.095
SO_3	5.91	3.995	9.995	4.61	2.039	11.544	3.57	0.87	13.949
Cl	0.52	0	1.628	1.19	0	4.398	0.57	0	2.756
F	–	–	0	–	–	0	–	–	0
H_2O	–	0.285	–	–	0.331	–	–	0.124	–
Proportion[a]	–	0.68643	0.31357	–	0.737	0.263	–	0.80035	0.19965

[a] These proportions represent the maximum possible proportion of crystalline material (upper limit) and, consequently, the minimum proportion of amorphous material (lower limit).

TABLE 10C. CheMin sample APXS, amorphous (normalized), and crystalline (normalized) compositions, in oxide wt%: Murray formation samples

	Confidence Hills			Mojave2			Telegraph Peak			Buckskin			Murray Average		
	APXS	Xtal	Amorph	APXS	Xtal	Amorph	APXS	Xtal	Amorph	APXS	Xtal	Amorph	APXS	Xtal	Amorph
SiO_2	48.13	45.372	53.23	49.48	43.652	55.725	52.7	52.592	52.986	73.65	71.064	75.934	55.99	53.17	59.469
TiO_2	1.13	0	3.135	1.19	0	2.487	1.23	0	5.859	1.57	0	2.81	1.28	0	3.573
Al_2O_3	9.73	12.028	5.708	11.43	15.281	7.196	10.74	13.086	1.881	5.66	12.884	0	9.39	13.32	3.696
Cr_2O_3	0.39	0	1.082	0.37	0	0.773	0.36	0	1.715	0.1	0	0.179	0.305	0	0.937
FeO_T	19.83	23.373	13.652	16.11	19.59	12.269	18.68	19.08	17.129	5.49	6.396	4.796	15.028	17.11	11.962
MnO	0.372	0	1.032	0.397	0	0.831	0.248	0	1.183	0.09	0	0.161	0.277	0	0.802
MgO	5.55	6	4.78	4.55	3.401	5.794	2.93	2.771	3.522	0.82	0	1.467	3.463	3.043	3.891
CaO	4.58	6.704	0.843	4.33	8.285	0	4.37	5.149	1.425	3.05	4.215	2.145	4.083	6.088	1.103
Na_2O	2.65	2.965	2.105	3.01	4.094	1.819	3.34	3.613	2.304	2.08	3.27	1.152	2.77	3.486	1.845
K_2O	0.98	1.536	0	0.73	0.379	1.111	0.98	1.24	0	0.96	1.108	0.847	0.913	1.066	0.49
P_2O_5	1.02	1.032	1.003	1.29	1.777	0.754	1.33	1.309	1.405	1.25	0	2.237	1.223	1.03	1.35
SO_3	4.86	0.672	12.293	6.27	2.528	10.342	2.54	0.78	9.162	4.8	1.063	7.754	4.618	1.261	9.888
Cl	0.41	0	1.137	0.43	0	0.899	0.3	0	1.429	0.29	0	0.519	0.358	0	0.996
F	–	–	0.092	–	–	0.159	–	–	0.117	–	–	0	–	–	0.092
H_2O	–	0.227	–	–	0.853	–	–	0.263	–	–	0	–	–	0.336	–
Proportion[a]	–	0.6496	0.3504	–	0.5322	0.4678	–	0.8034	0.1966	–	0.4421	0.5579	–	0.6068	0.3932

[a] These proportions represent the maximum possible proportion of crystalline material (upper limit) and, consequently, the minimum proportion of amorphous material (lower limit). Bulk crystalline and amorphous component compositions computed with FULLPAT-estimated proportions are reported in Morris et al. (2016) and Rampe et al. (2017).

TABLE 10D. CheMin sample APXS, amorphous (normalized), and crystalline (normalized) compositions, in oxide wt%: Stimson formation samples

	Big Sky			Greenhorn			Lubango			Okoruso			Stimson Average		
	APXS	Xtal[a]	Amorph	APXS	Xtal	Amorph	APXS	Xtal	Amorph	APXS	Xtal	Amorph	APXS	Xtal	Amorph
SiO_2	42.95	46.36	24.133	53.24	34.126	63.525	59.8	39.102	68	45.13	45.546	43.909	50.28	41.284	49.892
TiO_2	1	0	6.587	1	0	1.537	1.12	0	1.572	0.94	0	3.654	1.015	0	3.338
Al_2O_3	11.52	13.572	0.123	3.92	11.234	0	3.09	10.636	3.62	9.64	11.723	3.62	7.043	11.791	0.936
Cr_2O_3	0.51	0	3.359	0.45	0	0.692	0.29	0	0.407	0.41	0	1.594	0.415	0	1.513
FeO_T	21.55	22.299	17.478	15.25	24.763	10.159	8.22	16.543	4.792	22.4	24.381	16.668	16.855	21.997	12.274
MnO	0.401	0	2.641	0.137	0	0.211	0.09	0	0.126	0.39	0	1.516	0.255	0	1.124
MgO	7.49	6.21	14.676	1.81	2.461	1.462	1.55	3.192	0.874	8.97	7.04	14.539	4.955	4.726	7.888
CaO	6.12	7.222	0	7.8	12.155	5.47	8.23	12.35	6.516	6.37	5.824	7.943	7.13	9.388	4.982
Na_2O	3.08	2.554	6.03	2.43	3.093	2.076	1.92	3.694	1.189	3.08	3.026	3.235	2.628	3.092	3.133
K_2O	0.46	0.292	1.402	0.3	0	0.461	0.31	0	0.435	0.37	0.498	0	0.36	0.198	0.575
P_2O_5	0.72	0.548	1.686	1.15	0	1.767	1.33	0	1.867	0.75	0.675	0.966	0.988	0.306	1.572
SO_3	3.35	0.894	17.076	11.92	11.908	11.934	13.71	13.419	13.773	0.96	1.149	0.412	7.485	6.843	10.799
Cl	0.73	0	4.809	0.46	0	0.707	0.32	0	0.449	0.5	0	1.944	0.503	0	1.977
F	–	–	0.049	–	–	0	–	–	0	–	–	0.06	–	–	0.055
H_2O	–	0	–	–	0.259	–	–	1.064	–	–	0.077	–	–	0.467	–
Proportion[b]	–	0.85897	0.14103	–	0.35592	0.64408	–	0.2939	0.7061	–	0.7542	0.2458		0.5657	0.4343

[a] Raw Big Sky crystalline abundances (Yen et al. 2017) were used for the amorphous calculations rather than the contamination-subtracted abundances reported in Table 2.
[b] These proportions represent the maximum possible proportion of crystalline material (upper limit) and, consequently, the minimum proportion of amorphous material (lower limit). Bulk crystalline and amorphous component compositions computed with FULLPAT-estimated proportions are reported in Yen et al. (2017).

(Extended below)

Achilles et al. 2017; Yen et al. 2017). Therefore, characterizing the amorphous material is an important part of assessing the nature of ancient environments in Gale crater. Below, we provide several examples of the amorphous component compositions and their geologic implications.

The active dune material (Gobabeb) contains a high proportion of amorphous material (lower limit = ~42 wt%) with SiO_2, FeO, Al_2O_3, and SO_3 as its major constituent oxides (Table 10a). Possible phases responsible for this chemistry could include maskelynite, amorphous silica, nanophase iron oxides, and sulfates (Achilles et al. 2017). These phases suggest a history of impact, oxidation, aqueous, and likely physical (e.g., eolian) processes involved in the formation of the amorphous materials. The inactive, armored dune (Rocknest) has a lower amount of amorphous material (lower limit = ~20 wt%) and a significantly lower proportion of SiO_2 and Al_2O_3, but a much greater SO_3. The increased amount of SO_3 is attributed to the accumulation of wind-blown dust because of the inactivity of the Rocknest dune (Achilles et al. 2017). The disparity in SiO_2 content between the two soil samples is poorly understood, but we have observed that high SiO_2 proportions trends with high amorphous content in Gale crater samples; additionally, Achilles et al. (2017) proposes that the amorphous silica material in Gobabeb could be derived from the nearby Murray and altered Stimson strata. CheMin did not detect minerals containing P, Cl, Cr, Mn, and Ti; therefore, these elements are assumed to be incorporated with the X-ray amorphous component, but, as discussed previously, trace or minor amounts of these elements could be included in crystalline phases. Chlorine may be in the form of various salts of chlorides, perchlorates, and/or chlorates, but if present, these salts occur in quantities well below the detection limit of CheMin. Oxychlorine compounds (e.g., perchlorates and possibly chlorates) have been detected by the MSL Sam Analysis at Mars (SAM) instrument (Sutter et al. 2017). Cr, Mn, and Ti may be present in trace quantities in primary igneous phases (as discussed above) or as oxides and with other secondary alteration phases that are below the detection limit of CheMin. Likewise, no P-containing minerals were detected with CheMin, but may be

TABLE 10E. CheMin sample APXS, amorphous (normalized), and crystalline (normalized) compositions, in oxide wt%: Stimson formation samples

	Unaltered Stimson Average			Altered Stimson Average		
	APXS	Xtal	Amorph	APXS	Xtal	Amorph
SiO_2	44.04	45.953	34.021	56.52	36.614	65.763
TiO_2	0.97	0	5.121	1.06	0	1.555
Al_2O_3	10.58	12.648	1.872	3.505	10.935	0
Cr_2O_3	0.46	0	2.477	0.37	0	0.55
FeO_T	21.975	23.34	17.073	11.735	20.653	7.476
MnO	0.396	0	2.079	0.114	0	0.169
MgO	8.23	6.625	14.608	1.68	2.827	1.168
CaO	6.245	6.523	3.972	8.015	12.253	5.993
Na_2O	3.08	2.79	4.633	2.175	3.394	1.633
K_2O	0.415	0.395	0.701	0.305	0	0.448
P_2O_5	0.735	0.612	1.326	1.24	0	1.817
SO_3	2.155	1.022	8.744	12.815	12.664	12.854
Cl	0.615	0	3.377	0.39	0	0.578
F	–	–	0.055	–	–	0
H_2O	–	0.039	–	–	0.662	–
Proportion[a]	–	0.807	0.193	–	0.325	0.675

[a] These proportions represent the maximum possible proportion of crystalline material (upper limit) and, consequently, the minimum proportion of amorphous material (lower limit). Bulk crystalline and amorphous component compositions computed with FULLPAT-estimated proportions are reported in Yen et al. (2017).

present at quantities below the detection limit. Phosphorus may also be present in secondary alteration phases or chemisorbed on nanophase weathering products (e.g., Rampe et al. 2016).

The amorphous component of the Murray formation is somewhat similar to that of the scooped soils or the altered Stimson formation, with few noteworthy trends. An obvious exception is the Buckskin mudstone, which is composed predominately of SiO_2 (lower limit = ~76 wt%) along with SO_3 (~7.6 wt%), FeO_T (total Fe content calculated as FeO; ~4.8 wt%), TiO_2 (~2.8 wt%), and P_2O_5 (~2.2 wt%) as the most abundant oxides (Table 10c). Other elements (e.g., Cl) are also present as minor or trace quantities in the amorphous component (Table 10c). Possible candidate phases in the amorphous material are opal-A or high-Si glass, volatile-bearing mixed-cation sulfates, phosphates, and chlorides/perchlorates/chlorates, and Ti- and Fe-oxides (Morris et al. 2016). Opaline silica could have formed during diagenesis of high-SiO_2 glass or as a residue of acidic leaching of the sediments

or source sediments (Morris et al. 2016). The other secondary phases may have been derived during diagenesis from multiple episodes of aqueous alteration with varying solution compositions and temperatures.

The significantly greater average abundance of amorphous material in Greenhorn and Lubango samples (lower limits = ~64–71 wt%) vs. that of the Big Sky and Okoruso samples (lower limits = ~14–43 wt%) (Table 10e), supports the assertion that the former two Stimson samples have been altered while the latter are significantly less-so (or "unaltered") (Yen et al. 2017). As observed in the general trend of all Gale crater samples, the Stimson samples show that Si content, both in absolute abundance and normalized to amorphous-component abundance, increases with increasing amorphous-component proportion. The opposite trend is observed in Fe content. In the Stimson, these trends can likely be attributed to the partial dissolution of pyroxene, with plagioclase less affected by the alteration undergone by Greenhorn and Lubango. Magnetite abundance remains relatively constant throughout the Stimson samples, having been less affected by alteration or, alternatively, having been precipitated as a secondary phase during alteration (Yen et al. 2017). The ratios of plagioclase to magnetite remain relatively consistent across the Stimson, but the ratio of plagioclase to pyroxene is ~1.4 in unaltered Stimson and ~3.0 in altered Stimson samples, showing preferential dissolution of pyroxene. Note that small amounts of an alkali feldspar phase and fluorapatite were detected in Big Sky and Okoruso, but not in the altered Stimson samples; this absence could indicate that these phases were dissolved during alteration or they could simply be below the detection limit of the instrument. Unfortunately, the crystalline abundances of the alkali feldspar and fluorapatite are too low to make any meaningful comparison between the P and K contents of the crystalline and amorphous materials.

ACKNOWLEDGMENTS

REFERENCES CITED

Achilles, C.N., Downs, R.T., Ming, D.W., Rampe, E.B., Morris, R.V., Treiman, A.H., Morrison, S.M., Yen, A.S., Vaniman, D.T., Blake, D.F., and others. (2017) Mineralogy of an active eolian sediment from the Namib dune, Gale crater, Mars. Journal of Geophysical Research: Planets, 122, 2344–2361.

Allison, M. (1997) Accurate analytic representations of solar time and seasons on Mars with applications to the Pathfinder/Surveyor missions. Geophysical Research Letters, 24, 1967–1970.

Anderson, R.C., Jandura, L., Okon, A.B., Sunshine, D., Roumeliotis, C., Beegle, L.W., Horowitz, J., Kennedy, B., Limonadi, D., McCloskey, S., and others. (2012) Collecting Samples in Gale crater, mars; an overview of the Mars Science Laboratory Sample acquisition, sample processing and handling system. Space Science Reviews, 170, 57–75.

Angel, R.J., Ross, N.L., Zhao, J., Sochalski-Kolbus, L., Krüger, H., and Schmidt, B.C. (2013) Structural controls on the anisotropy of tetrahedral frameworks: the example of monoclinic feldspars. European Journal of Mineralogy, 25(4), 597–614.

Baker, M.B., and Beckett, J.R. (1999) The origin of abyssal peridotites: a reinterpretation of constraints based on primary bulk compositions. Earth and Planetary Science Letters, 171(1), 49–61.

Bambauer, H.U., Corlett, M., Eberhard, E., and Viswanathan, K. (1967) Diagrams for the determination of plagioclases using X-ray powder methods (Part III of laboratory investigations of plagioclases). Schweizerische Mineralogische und Petrographische Mitteilungen, 47, 333–349.

Bish, D.L., Blake, D.F., Vaniman, D.T., Chipera, S.J., Morris, R.V., Ming, D.W., Treiman, A.H., Sarrazin, P., Morrison, S.M., Downs, R.T., and others and MSL Science Team. (2013) X-ray diffraction results from Mars Science Laboratory: mineralogy of Rocknest at Gale crater. Science, 27, 341, 1238932.

Blake, D., Vaniman, D., Achilles, C., Anderson, R., Bish, D., Bristow, T., Chen, C., Chipera, S., Crisp, J., Des Marais, D., and others. (2012) Characterization and calibration of the CheMin mineralogical instrument on Mars Science Laboratory. Space Science Reviews, 170, 341–399.

Blake, D.F., Morris, R.V., Kocurek, G., Morrison, S.M., Downs, R.T., Bish, D.L., Ming, D.W., Edgett, K.S., Rubin, D., Goetz, W., and others and MSL Science Team. (2013) Curiosity at Gale crater, Mars: characterization and analysis of the Rocknest sand shadow. Science, 341, 1239505.

Bristow, T.F., Bish, D.L., Vaniman, D.T., Morris, R.V., Blake, D.F., Grotzinger, J.P., Rampe, E.B., Crisp, J.A., Achilles, C.N., Ming, D.W., and others. (2015) The origin and implications of clay minerals from Yellowknife Bay, Gale crater, Mars. American Mineralogist, 100, 824–836.

Campbell, J.L., Perrett, G.M., Gellert, R., Andrushenko, S.M., Boyd, N.I., Maxwell, J.A., King, P.l, and Schofield, Celest D.M. (2012) Calibration of the Mars Science Laboratory Alpha Particle X-ray Spectrometer.Space Science Reviews, 170, 319–340.

Chipera, S.J., and Bish, D.L. (2002) FULLPAT: A full-pattern quantitative analysis program for X-ray powder diffraction using measured and calculated patterns. Journal of Applied Crystallography, 35, 744–749.

——— (2013) Fitting full X-ray diffraction patterns for quantitative analysis: a method for readily quantifying crystalline and disordered phases. Advances in Materials Physics and Chemistry, 3, 47–53.

Christensen, P.R., Jakosky, B.M., Kieffer, H.H., Malin, M.C., McSween, H.Y., Nealson, K., Mehall, G.L., Silverman, S.H., Ferry, S., Caplinger, M., and Ravine, M. (2004a) The thermal emission imaging system (THEMIS) for the Mars 2001 Odyssey Mission. Space Science Reviews, 110(1-2), 85–130.

Christensen, P.R., Wyatt, M.B., Glotch, T.D., Rogers, A.D., Anwar, S., Arvidson, R.E., Bandfield, J.L., Blaney, D.L., Budney, C., Calvin, W.M., and Fallacaro, A. (2004b) Mineralogy at Meridiani Planum from the Mini-TES experiment on the Opportunity Rover. Science, 306(5702), 1733–1739.

Clark, B.C., Morris, R.V., McLennan, S.M., Gellert, R., Jolliff, B., Knoll, A.H., Squyres, S.W., Lowenstein, T.K., Ming, D.W., Tosca, N.J., and Yen, A. (2005) Chemistry and mineralogy of outcrops at Meridiani Planum. Earth and Planetary Science Letters, 240(1), 73–94.

Dal Negro, A., De Pieri, R., Quareni, S., and Taylor, W.H. (1978) The crystal structures of nine K feldspars from Adamello Massiff (Northern Italy). Acta Crystallographica, B34, 2699–2707.

Dehouck, E., McLennan, S.M., Meslin, P.-Y., and Cousin, A. (2014) Constraints on abundance, composition, and nature of X-ray amorphous components of soils and rocks at Gale crater, Mars. Journal of Geophysical Research: Planets, 119, 2640–2657.

Dera, P., Zhuravlev, K., Prakapenka, V., Rivers, M.L., Finkelstein, G.J., Grubor-Urosevic, O., Tschauner, O., Clark, S.M., and Downs, R.T. (2013) High pressure single-crystal micro X-ray diffraction analysis with GSE_ADA/RSV software. High Pressure Research, 33, 466–484.

Filiberto, J., and Dasgupta, R. (2015) Constraints on the depth and thermal vigor of melting in the Martian mantle. Journal of Geophysical Research: Planets, 120, 109–122.

Gellert, R., Clark, B.C. III, MSL and MER Science Teams (2015) Compositional measurements of rocks and soils on NASA's Mars rovers with the alpha-particle X-ray spectrometer (APXS). Elements, 11, 39–44.

Golden, D.C., Ming, D.W., Morris, R.V., and Graff, T.G. (2008) Hydrothermal synthesis of hematite spherules and jarosite—Implications for diagenesis and hematite spherule formation in sulphate outcrops at Meridiani Planum, Mars. American Mineralogist, 93, 1201–1214.

Grotzinger, J.P. (2013) Analysis of surface materials by the Curiosity Mars rover. Science, 341, 1475.

Grotzinger, J.P., Sumner, D.Y., Kah, L.C., Stack, K., Gupta, S., Edgar, L., Rubin, D., Lewis, K., Schieber, J., Mangold, N., and others. (2014) A habitable fluvio-lacustrine environment at Yellowknife Bay, Gale crater, Mars. Science, 343, 1242777.

Gupta, A.K. (2015) Origin of Potassium-Rich Silica-Deficient Igneous Rocks, 536 p. Springer, New York.

Hewins, R.H., Zanda, B., Humayun, M., Nemchin, A., Lorand, J.P., Pont, S., Deldicque, D., Bellucci, J.J., Beck, P., Leroux, H., and Marinova, M. (2017) Regolith breccia Northwest Africa 7533: Mineralogy and petrology with implications for early Mars. Meteoritics & Planetary Science, 52(1), 89–124.

Hurowitz, J.A., Grotzinger, J.P., Fischer, W.W., McLennan, S.M., Milliken, R.E., Stein, N., Vasavada, A.R., Blake, D.F., Dehouck, E., Eigenbrode, J.L., and Fairén, A.G. (2017) Redox stratification of an ancient lake in Gale crater, Mars. Science, 356, 6849.

Klingelhöfer, G., Morris, R.V, Bernhardt, B., Schröder, C., Rodionov, D.S., de Souza, P.A., Yen, A., Gellert, R., Evlanov, E.N., Zubkov, B., and others. (2004) Jarosite and hematite at Meridiani Planum from Opportunity's Mössbauer Spectrometer. Science, 306, 1740–1745.

Kuehner, S.M., and Joswiak, D.J. (1996) Naturally occurring ferric iron sanidine from the Leucite Hills lamproite. American Mineralogist, 81, 229–237.

Le Deit, L., Mangold, N., Forni, O., Cousin, A., Lasue, J., Schroder, S., Wiens, R.C., Sumner, D., Fabre, C., Stack, K.M., and others. (2016) The potassic sedimentary rocks in Gale crater, Mars, as seen by ChemCam on board Curiosity. Journal of Geophysical Research: Planets, 121, 784–804.

Lebedeva, Y.S., Pushcharovsky, D.Y., Pasero, M., Merlino, S., Kashaev, A.A., Taroev, V.K., Linthout, K., and Lustenhouwer, W.J. (1993) Ferrian high sanidine in a lamproite from Cancarix, Spain. Mineralogical magazine, 57(2), 289–299.

Lee, C.-T.A., Luffi, P., Plank, T., Dalton, H., and Leeman, W.P. (2009) Constraints on the depths and temperatures of basaltic magma generation on Earth and other terrestrial planets using new thermobarometers for mafic magmas. Earth and Planetary Science Letters, 279, 20–33.

Lindsley, D.H. (1983) Pyroxene thermometry. American Mineralogist, 68, 477–493.

McSween, H.Y., and Treiman, A.H. (1998) Martian meteorites. In J.J. Papike, Ed., Planetary Materials, 36(1), 6-01–6-54. Reviews in Mineralogy, Mineralogical Society of America, Chantilly, Virginia.

Mills, S.J., Nestola, F., Kahlenberg, V., Christy, A.G., Hejny, C., and Redhammer, G.J. (2013) Looking for jarosite on Mars: the low-temperature crystal structure of jarosite. American Mineralogist, 98, 1966–1971.

Morris, R.V., Klingelhöfer, G., Schröder, C., Rodionov, D.S., Yen, A., Ming, D.W., de Souza, P.A., Wdowiak, T., Fleischer, I., Gellert, R., and others. (2006) Mössbauer mineralogy of rock, soil, and dust at Meridiani Planum, Mars: Opportunity's journey across sulfate-rich outcrop, basaltic sand and dust, and hematite lag deposits. Journal of Geophysical Research: Planets, 111, E12S15.

Morris, R.V., Klingelhöfer, G., Schröder, C., Fleischer, I., Ming, D.W., Yen, A.S., Gellert, R., Arvidson, R.E., Rodionov, D.S., Crumpler, L.S., and others. (2008) Iron mineralogy and aqueous alteration from Husband Hill through Home Plate at Gusev Crater, Mars: results from the Mössbauer instrument on the Spirit Mars Exploration Rover. Journal of Geophysical Research: Planets, 113, E12S42.

Morris, R.V., Vaniman, D.T., Blake, D.F., Gellert, R., Chipera, S.J., Rampe, E.B., Ming, D.W., Morrison, S.M., Downs, R.T., Treiman, A.H., and others. (2016) Silicic volcanism on Mars evidenced by tridymite in high-SiO₂ sedimentary rock at Gale crater. Proceedings of the National Academy of Sciences, 113, 7071–7076.

Morrison, S.M., Downs, R.T., Blake, D.F., Prabhu, A., Eleish, A., Vaniman, D.T., Ming, D.W., Rampe, E.B., Bristow, T.F., and Achilles, C.N. (2018) Relationships between unit-cell parameters and composition for rock-forming minerals on Earth, Mars, and other extraterrestrial bodies. American Mineralogist, 103, 849–857.

Nyquist, L.E., Shih, C.Y., McCubbin, F.M., Santos, A.R., Shearer, C.K., Peng, Z.X., Burger, P.V., and Agee, C.B. (2016) Rb-Sr and Sm-Nd isotopic and REE studies of igneous components in the bulk matrix domain of Martian breccia Northwest Africa 7034. Meteoritics & Planetary Science, 51(3), 483–498.

O'Connell-Cooper, C.D., Spray, J.G., Thompson, L.M., Gellert, R., Berger, J.A., Boyd, N.I., Desouza, E.D., Perrett, G.M., Schmidt, M., and VanBommel, S.J. (2017) APXS-derived chemistry of the Bagnold dune sands: Comparisons with Gale Crater soils and the global Martian average, Journal of Geophysical Research, Planets, 122, 2623–2643.

Papike, J.J., Karner, J.M., Shearer, C.K., and Burger, P. V (2009) Silicate mineralogy of martian meteorites. Geochimica et Cosmochimica Acta, 73, 7443–7485.

Rampe, E.B., Morris, R.V., Ruff, S.W., Horgan, B., Dehouck, E., Achilles, C.N., Ming, D.W., Bish, D.L., and Chipera, S.J. (2014) Amorphous phases on the surface of Mars. Eighth International Conference on Mars (2014), 1–2.

Rampe, E.B., Morris, R.V., Archer, P.D., Agresti, D.G. Jr., and Ming, D.W. (2016) Recognizing sulfate and phosphate complexes chemisorbed onto nanophase weathering products on Mars using in-situ and remote observations. American Mineralogist, 101, 678–689.

Rampe, E.B., Ming, D.W., Blake, D.F., Vaniman, D.T., Chipera, S.J., Bristow, T.F., Morris, R.V., Yen, A.S., Morrison, S.M., Grotzinger, J.P., and others. (2017) Mineralogical trends in mudstones from the Murray formation, Gale crater, Mars. Earth and Planetary Science Letters, 471, 172–185.

Ruff, S.W., Christensen, P.R., Glotch, T.D., Blaney, D.L., Moersch, J.E., and Wyatt, M.B. (2008) The mineralogy of Gusev crater and Meridiani Planum derived from the Miniature Thermal Emission Spectrometers on the Spirit and Opportunity rovers. In J.F. Bell III, Ed., The Martian Surface: Composition, Mineralogy, and Physical Properties. Cambridge University Press, p. 315–338.

Sack, R.O. (1980) Some constraints on the thermodynamic mixing properties of Fe-Mg orthopyroxenes and olivines. Contributions to Mineralogy and Petrology, 71, 257–269.

Santos, A.R., Agee, C.B., McCubbin, F.M., Shearer, C.K., Burger, P.V., Tartese, R., and Anand, M. (2015) Petrology of igneous clasts in Northwest Africa 7034: Implications for the petrologic diversity of the Martian crust. Geochimica et Cosmochimica Acta, 157, 56–85.

Siebach, K.L., Baker, M.B., Grotzinger, J.P., McLennan, S.M., Gellert, R., Thompson, L.M., and Hurowitz, J.A. (2017) Sorting out compositional trends in sedimentary rocks of the Bradbury group (Aeolis Palus), Gale crater, Mars. Journal of Geophysical Research: Planets, 122(2), 295–328.

Sutter, B., McAdam, A.C., Mahaffy, P.R., Ming, D.W., Edgett, K.S., Rampe, E.B., Eigenbrode, J.L., Franz, H.B., Freissinet, C., Grotzinger, J.P., and Steele, A. (2017) Evolved gas analyses of sedimentary rocks and eolian sediment in Gale Crater, Mars: Results of the Curiosity Rover's Sample Analysis at Mars (SAM) Instrument from Yellowknife Bay to the Namib Dune. Journal of Geophysical Research: Planets, in press, DOI: 10.1002/2016JE005225.

Swayze, G.A., Desborough, G.A., Smith, K.S., Lowers, H.A., Hammarstrom, J.M., Diehl, S.F., Leinz, R.W., and Driscoll, R.H. (2008) Understanding jarosite—From mine waste to Mars. Understanding contaminants associated with mineral deposits, In P.L. Verplanck, Ed., Understanding Contaminants Associated with Mineral Deposits, U.S. Geological Survey Circular, 1328, 8–13.

Thompson, L.M., Schmidt, M.E., Spray, J.G., Berger, J.A., Faréin, A., Campbell, J.L., Perrett, G.M., Boyd, N., Gellert, R., Pradler, I., and VanBommel, S.J. (2016) Potassium-rich sandstones on Mars, Gale crater: the APXS perspective. Journal of Geophysical Research: Planets, 121, 1980–2003.

Treiman, A.H. (2005) The nakhlite martian meteorites: Augite-rich igneous rock from Mars. Chemie der Erde, 65, 203–270.

Treiman, A.H., and Medard, E. (2016) Mantle metasomatism in Mars: potassic basaltic sandstone in Gale crater derived from partial melt of phlogopite-peridotite. Geological Society of America Abstracts with Programs, Paper no. 49-12.

Treiman, A.H., Morris, R.V., Agresti, D.G., Graff, T.G., Achilles, C.N., Rampe, E.B., Bristow, T.F., Ming, D.W., Blake, D.F., Bish, D.L., and others. (2014) Ferrian saponite from the Santa Monica Mountains (California, U.S.A., Earth): Characterization as an analog for clay minerals on Mars with application to Yellowknife Bay in Gale crater. American Mineralogist, 99, 2234–2250.

Treiman, A.H., Bish, D.L., Vaniman, D.T., Chipera, S.J., Blake, D.F., Ming, D.W., Morris, R.V., Bristow, T.F., Morrison, S.M., Baker, M.B., and others. (2016) Mineralogy, provenance, and diagenesis of a potassic basaltic sandstone on Mars: CheMin X-ray diffraction of the Windjana sample (Kimberley area, Gale Crater). Journal of Geophysical Research: Planets, 121, 75–106.

Turnock, A.C., Lindsley, D.H., and Grover, J.E. (1973) Synthesis and unit cell parameters of Ca-Mg-Fe pyroxenes. American Mineralogist, 58, 50–59.

Vaniman, D.T., Bish, D.L., Ming, D.W., Bristow, T.F., Morris, R.V., Blake, D.F., Chipera, S.J., Morrison, S.M., Treiman, A.H., Rampe, E.B., and others and MSL Science Team. (2014) Mineralogy of a mudstone at Yellowknife Bay, Gale crater, Mars. Science, 343, 1243480.

Wittmann, A., Korotev, R.L., Jolliff, B.L., Irving, A.J., Moser, D.E., Barker, I., and Rumble, D. (2015) Petrography and composition of Martian regolith breccia meteorite Northwest Africa 7475. Meteoritics & Planetary Science, 50(2), 326–352.

Yen, A.S., Ming, D.W., Vaniman, D.T., Gellert, R., Blake, D.F., Morris, R.V., Morrison, S.M., Downs, R.T., Bristow, T.F., Clark, B.C., and others and the MSL Science Team. (2017) Multiple episodes of aqueous alteration along fractures in mudstone and sandstone in Gale crater, Mars. Earth and Planetary Science Letters, 471, 186–198.

Young, R.A., Ed. (1993) The Rietveld Method, International Union of Crystallography, 298 p. Oxford University Press.

Zolotov, M.Y., and Shock, E.L. (2005) Formation of jarosite-bearing deposits through aqueous oxidation of pyrite at Meridiani Planum, Mars. Geophysical Research Letters, 32, L21203.

Endnote: